Satellite Products and Services Review Board

Algorithm Theoretical Basis Document For NOAA VIIRS Surface Type

Compiled by the
SPSRB Common Standards Working Group

TITLE: VIIRS SURFACE TYPE ALGORITHM THEORETICAL BASIS DOCUMENT

AUTHORS:

Chengquan Huang (University of Maryland)

Xiwu Zhan (NESDIS Center for Satellite Applications and Research)

Ivan Csiszar (NESDIS Center for Satellite Applications and Research)

DOCUMENT HISTORY
DOCUMENT REVISION LOG

The Document Revision Log identifies the series of revisions to this document since the baseline release. Please refer to the above page for version number information.

DOCUMENT TITLE: NOAA VIIRS Surface Type Algorithm Theoretical Basis Document			
DOCUMENT CHANGE HISTORY			
Revision No.	**Date**	**Revision Originator Project Group**	**CCR Approval # and Date**
1.0	Sept 2018		
2.0	Sept. 2020	Address synergy of NOAA-20 and S-NPP for surface type monitoring (section 2.8)	
2.1	Sept. 2022	Added accuracy information for the AST 2021 product	

LIST OF CHANGES

Significant alterations made to this document are annotated in the List of Changes table.

DOCUMENT TITLE: NOAA VIIRS Surface Type Algorithm Theoretical Basis Document					
LIST OF CHANGE-AFFECTED PAGES/SECTIONS/APPENDICES					
Version Number	Date	Changed By	Page	Section	Description of Change(s)
2.1	Sept. 2022	C. Huang	43, 45	2.8	Added accuracy information for the AST 2021 product.

TABLE OF CONTENTS

LIST OF TABLES AND FIGURES

1. INTRODUCTION

Surface type is defined as the predominant type of surface cover in a given area. It is synonymous to land cover, which is commonly used in the remote sensing literature. In this document, the two terms will be used interchangeably. Surface type information is required as input to weather, climate, and hydrological models supporting various U.S. Government and academic customers (Hasager et al. 2003; Wilson and Henderson-Sellers 1985). Many biophysical variables important for these studies, including albedo, surface roughness, evapotranspiration, and respiration, are surface type dependent (Bright 2015; Hasager et al. 2003; Sellers et al. 1996; Townshend et al. 1994). These parameters control the transfer of energy, momentum, mass, and latent and sensible heat between the biosphere and the lower layers of the atmosphere (Chen and Dudhia 2001; Dickinson 1995; Sellers et al. 1995; Xue et al. 2001). Therefore, accurate representation of surface types and conditions is a key requirement for advancing the study of important elements of the earth systems, including weather and climate (Mahmood et al. 2014; Salazar et al. 2015), biogeochemical cycles (Bright 2015), and hydrological processes (Wood 1991; Zhou et al. 2015). Further, reliable and up-to-date information on surface type change is needed for land management (Luyssaert et al. 2014), implementation of national and international policies related to bio-diversity and climate change (Sexton et al. 2016; Venter et al. 2016), and many other applications (Mantyka-Pringle et al. 2016; Senapathi et al. 2015).

Land cover classification has a significant heritage in the remote sensing literature (Hansen and Loveland 2012; Townshend 1992). For nearly half a century, land cover products have been derived using data acquired by Landsat, the Système Probatoire pour l'Observation de la Terre (SPOT), and other observing systems, often at local to regional scales (Franklin and Wulder 2002; Townshend et al. 1991). At the globe scale, use of Landsat class data to derive land cover classifications at sub-hectare spatial resolutions has not been possible until recent years (Chen et al. 2015; Gong et al. 2013). Land cover products for model studies of weather and climate systems as well as other regional to global scale applications have been derived mainly using global observing systems, including the Advanced Very High Resolution Radiometer (AVHRR) onboard the NOAA-n satellite series (Hansen et al. 2000; Loveland et al. 2000), the Moderate Resolution Imaging Spectroradiometer (MODIS) launched as a part of the National Aeronautics and Space Administration (NASA) Earth Observing System (EOS) (Friedl et al. 2010; Friedl et al. 2002), and Satellite Pour l'Observation de la Terre Vegetation (SPOT Vegetation) (Bartholome and Belward 2005).

New and enhanced global observations has been and will continue to be collected from the Visible/Infrared Imager/Radiometer Suite (VIIRS). This instrument has been successfully deployed onboard two satellites – the S-NPP launched in 2011 and the first Joint Polar Satellite System (JPSS-1, which was renamed NOAA-20 soon after launch) in 2017, and

will be flown in future JPSS satellites[1]. Surface type is one of the environmental data records listed in the JPSS Level 1 Requirement Document (L1RD). This Algorithm Theoretical Basis Document (ATBD) describes the algorithms and production of the JPSS VIIRS Surface Type products.

1.1. Product Overview

1.1.1. Product Description

The original VIIRS Surface Type product was designed to be an Environmental Data Record (EDR). It is created for each VIIRS swath by redelivering (i.e., remapping) a gridded Quarterly Surface Type (QST) Intermediate Product (IP) for that swath. If fire and/or snow are detected (by the Active Fire and Snow EDR algorithms, respectively) at some or all pixel locations within that swath, those pixels are flagged in the Surface Type EDR QA data layer. The Surface Type EDR has been generated in the Interface Data Processing Segment (IDPS) implemented by Raytheon Company. The IDPS Surface Type EDR ATBD can be found at https://www.star.nesdis.noaa.gov/jpss/documents/ATBD/D0001-M01-S01-024_JPSS_ATBD_VIIRS-Surface-Type_A.pdf.

The QST IP is generated based on heritage algorithms used to produce global land cover products using MODIS and AVHRR data. It uses VIIRS observations acquired over a 12-month period, but is produced on a rolling quarterly basis. It is expected that these quarterly IPs could be used to capture some intra- and inter-annual surface type changes over large areas. Soon after the launch of the S-NPP, however, it was determined that it was unrealistic to expect that intra-annual surface type changes could be quantified using QST IPs produced within the same year, because the errors in these products likely would result in large quantities of spurious changes that would far exceed the amount of real changes (Friedl et al. 2010; Stow et al. 1980). Based on this observation, the QST IP is replaced with a static global gridded surface type map generated annually. The static product is then renamed the Annual Surface Type (AST) product and generated offline by the NESDIS STAR VIIRS Science Team.

The VIIRS Surface Type EDR provided in VIIRS swath space was primarily used by the VIIRS Land Surface Temperature (LST) EDR as an essential input. Changes were made to the LST EDR algorithm implemented in the S-NPP Data Exploration (NDE) system at NESDIS Environmental Satellite Processing Center (ESPC). The new algorithm does not require the Surface Type EDR, but a static surface type map is still needed. Consequently, the current JPSS L1RD for surface type only includes the Annual Surface Type (AST) product. The VIIRS AST product remains to be generated offline from NDE system, but the task to generate the Surface Type EDR to provide near real time surface type change data

---

[1] Updates on future JPSS missions are available at https://www.jpss.noaa.gov/mission_and_instruments.html.

has been dropped. Figure 1-1 shows the relationships between the IDPS Surface Type EDR and the current STAR-JPSS Offline Annual Surface Type (AST) product.
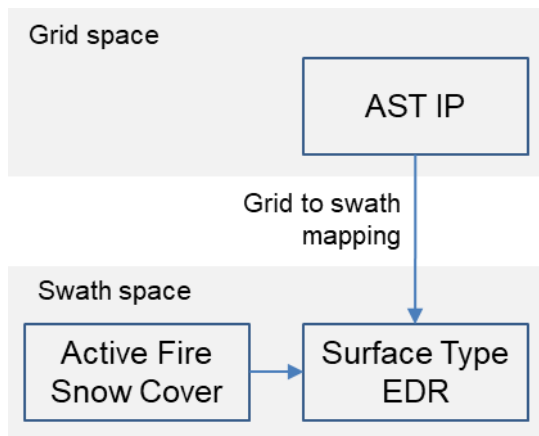
Figure 1-1. Relationship between the original IDPS Surface Type EDR and the Annual Surface Type (AST) product generated offline from the NDE system. AST was an Intermediate Product (IP) in the IDPS Surface Type EDR

1.1.2. Product Requirements

The Level 1 requirements for the VIIRS Surface Type product as described in the L1RD document were designed based on the original Surface Type EDR concept. Despite the above described changes to the surface type EDR and QST IP, these requirements remain applicable to the current implementation of the AST product (Table 1-1).

Table 1-1. Level requirements for the VIIRS Surface Type product

Subject	Threshold Value
a. Horizontal Cell Size [HCS, VIIRS Guarantee]	1 km
b. Horizontal Reporting Interval [VIIRS Guarantee]	HCS
c. Horizontal Coverage [VIIRS Guarantee]	Land
d. Measurement Range	17 IGBP Types Specified in Table 1-2
e. Correct Typing Probability (Vegetation /Surface Type) [VIIRS Guarantee]	> 70% for the 17 types.

Many classification schemes have been developed for representing the wide range of surface types across the globe. The VIIRS AST product uses the 17-class scheme developed by the International Geosphere Biosphere Program (IGBP). The definitions of those classes are provided in Table 1-2.

Table 1-2. IGBP surface type definitions (Belward and Loveland 1996).

IGBP Surface Type Number and Name	Definition
1) Evergreen Needleleaf Forests	Lands dominated by woody vegetation with a percent cover >60% and height exceeding 2 meters. Almost all trees remain green all year. Canopy is never without green foliage.
2) Evergreen Broadleaf Forests	Lands dominated by woody vegetation with a percent cover >60% and height exceeding 2 meters. Almost all trees and shrubs remain green year round. Canopy is never without green foliage.
3) Deciduous Needleleaf Forests	Lands dominated by woody vegetation with a percent cover >60% and height exceeding 2 meters. Consists of seasonal needleleaf tree communities with an annual cycle of leaf-on and leaf-off periods.
4) Deciduous Broadleaf Forests	Lands dominated by woody vegetation with a percent cover >60% and height exceeding 2 meters. Consists of broadleaf tree communities with an annual cycle of leaf-on and leaf-off periods.
5) Mixed Forests	Lands dominated by trees with a percent cover >60% and height exceeding 2 meters. Consists of tree communities with interspersed mixtures or mosaics of the other four forest types. None of the forest types exceeds 60% of landscape.
6) Closed Shrublands	Lands with woody vegetation less than 2 meters tall and with shrub canopy cover >60%. The shrub foliage can be either evergreen or deciduous.
7) Open Shrublands	Lands with woody vegetation less than 2 meters tall and with shrub canopy cover between 10-60%. The shrub foliage can be either evergreen or deciduous.
8) Woody Savannas	Lands with herbaceous and other understory systems, and with forest canopy cover between 30-60%. The forest cover height exceeds 2 meters.
9) Savannas	Lands with herbaceous and other understory systems, and with forest canopy cover between 10-30%. The forest cover height exceeds 2 meters.
10) Grasslands	Lands with herbaceous types of cover. Tree and shrub cover is less than 10%.
11) Permanent Wetlands	Lands with a permanent mixture of water and herbaceous or woody vegetation. The vegetation can be present in either salt, brackish, or fresh water.
12) Croplands	Lands covered with temporary crops followed by harvest and a bare soil period (*e.g.*, single and multiple cropping systems). Note that perennial woody crops will be classified as the appropriate forest or shrub land cover type.
13) Urban and Built-Up Lands	Lands covered by buildings and other man-made structures.
14) Cropland/Natural Vegetation Mosaics	Lands with a mosaic of croplands, forests, shrubland, and grasslands in which no one component comprises more than 60% of the landscape.
15) Snow and Ice	Lands under snow/ice cover throughout the year.
16) Barren	Lands with exposed soil, sand, rocks, or snow and never has more than 10% vegetated cover during any time of the year.
17) Water Bodies	Oceans, seas, lakes, reservoirs, and rivers. Can be either fresh or salt-water bodies.

1.2. Satellite Instrument Description

The VIIRS instrument has 22 spectral bands within the visible-infrared-thermal spectral range, including 16 moderate (M) bands having a nadir resolution of 750-m, one day-and-night band (DNB) with a near constant 750-m resolution across the full scan, and 5 imagery (I) bands having a 375-m nadir resolution. A comparison of these bands with those of other instruments, including MODIS, AVHRR, and Landsat Thematic Mapper (TM) is shown in Table 1-3.

Table 1-3. Inter-comparison of the Spectral Bands of VIIRS, MODIS, AVHRR, and TM

VIIRS			MODIS Equivalent			AVHRR Equivalent (AVHRR-3)			TM Equivalent (Landsat 4 & 5)		
VIIRS Band	Spectral Range (um)	Nadir HSR (m)	Band	Range	HSR	Band	Range	HSR	Band	Range	HSR
M1	0.400-0.421	750	8	0.405-0.420	1000						
M2	0.436-0.451	750	9	0.438-0.448	1000						
M3	0.477-0.496	750	10	0.483-0.493	1000				1	0.450-0.520	30
M4	0.541-0.561	750	4	0.545-0.565	500				2	0.520-0.600	30
I1	0.597-0.679	375	1	0.620-0.670	250	1	0.572-0.703	1100	3	0.630-0.690	30
M5	0.662-0.680	750	1	0.620-0.670	250	1	0.572-0.703	1100	3	0.630-0.690	30
DNB	0.5 - 0.9	750									
M6	0.733-0.752	750	15	0.743-0.753	1000						
M7/I2	0.843-0.881	750/375	2	0.841-0.876	250	2	0.720-1.000	1100	4	0.760-0.900	30
M8	1.225-1.252	750	5	SAME	500						
M9	1.368-1.383	750	26	1.360-1.390	1000						
M10/I3	1.571-1.631	750/375	6	1.628-1.652	500	3a	SAME	1100	5	1.550-1.750	30
M11	2.234-2.280	750	7	2.105-2.155	500				7	2.080-2.350	30
I4	3.550-3.937	375	20	3.660-3.840	1000	3b	SAME	1100			
M12	3.598-3.791	750	20	SAME	1000	3b	3.550-3.930	1100			
M13	3.987-4.145	750	21-23	3.929-4.080	1000						
M14	8.407-8.748	750	29	SAME	1000						
M15	10.23-11.25	750	31	10.78-11.28	1000	4	10.3-11.3	1100	6	10.40-12.50	120
I5	10.56-12.43	375	32	11.77-12.27	1000	5	11.5-12.5	1100	7	10.40-12.50	120
M16	11.41-12.32	750	32	11.77-12.27	1000	5	11.5-12.5	1100	8	10.40-12.50	120

The M bands are used to produce the 1 km VIIRS AST product as specified in Table 1-1. Unlike MODIS, whose pixel size at the end of a scan line can be up to 5 times larger than at nadir in the scan direction, VIIRS uses a two-stage aggregation scheme to constrain pixel size increases along the scan line to within 2 times of a nadir pixel (Figure 1-2). It has

been demonstrated that with this aggregation scheme, the effective spatial resolution of gridded VIIRS data is close to the 1 km spatial resolution of the AST product specified in Table 1-1 (Campagnolo et al. 2016).
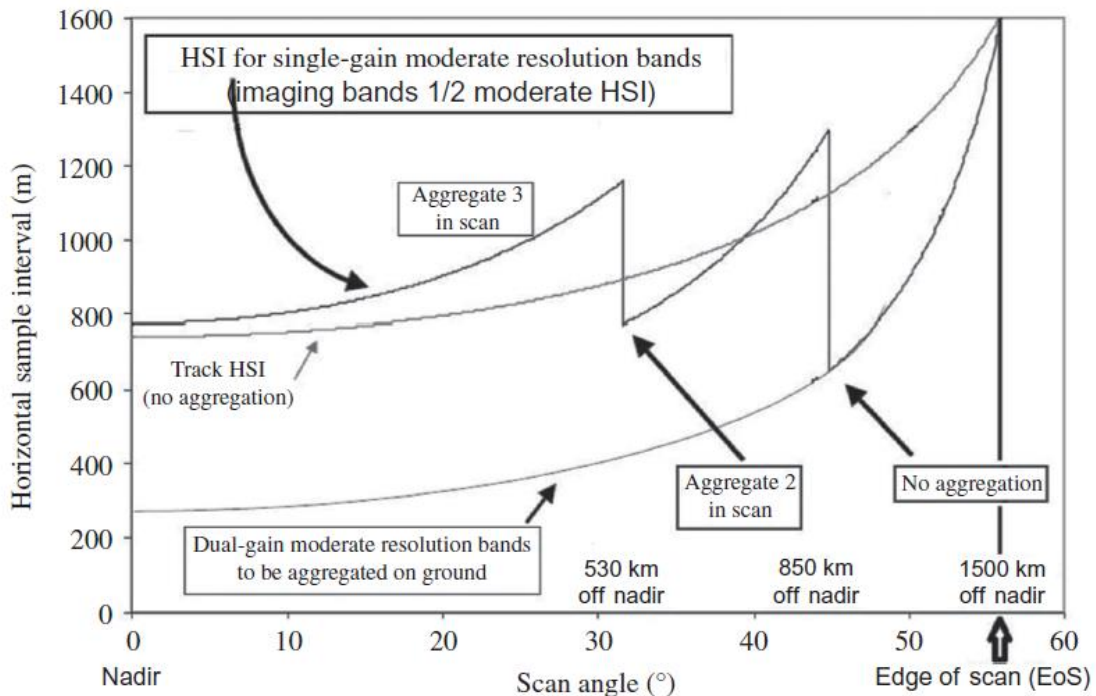
Figure 1-2. VIIRS uses a 2-stage aggregation scheme to constrain the pixel size at the end of a scan line within about 2 times of a nadir pixel in the scan direction. Without such an aggregation scheme, a MODIS pixel at the end of a scan line is about 5 times the size of a nadir pixel in the scan direction (from (Schueler et al. 2013)).

2. ALGORITHM DESCRIPTION

The VIIRS Annual Surface Type (AST) algorithm is based on approaches developed for generating global land cover products from MODIS and AVHRR (Friedl et al. 2010; Friedl et al. 2002; Hansen et al. 2000; Loveland et al. 2000). These approaches require gridded global composites of satellite images as inputs, which are used to produce metrics designed to provide more consistent representation of the spectral-temporal signatures of different surface types across the globe than the original observations or composites. The derived metrics are then classified to produce global land cover maps using classification models derived using machine learning algorithms and globally representative training samples.

For MODIS, gridded composites are generated by the MODIS Adaptive Processing System (MODAPS) and are provided as a standard product for use by downstream applications, including the generation of global land cover products. For VIIRS, gridded composites are not available as a stand product. Generating these composites is part of the VIIRS AST processing flow.

2.1. Processing Outline

The VIIRS AST processing flow includes two major steps: VIIRS data preprocessing and surface type classification/validation (Figure 2-1). During preprocessing, swath level observations are mapped into the global Sinusoidal grid space. The Sinusoidal projection is the standard projection for most MODIS products (Wolfe et al. 1998), and is the designated projection for the VIIRS AST product. The gridded VIIRS data are then used to create a global mosaic for each day. These daily composites are further composited to create monthly composites to minimize contaminations by clouds, shadows, or other bad observations. Finally, the monthly composites are used to create a suite of annual metrics.
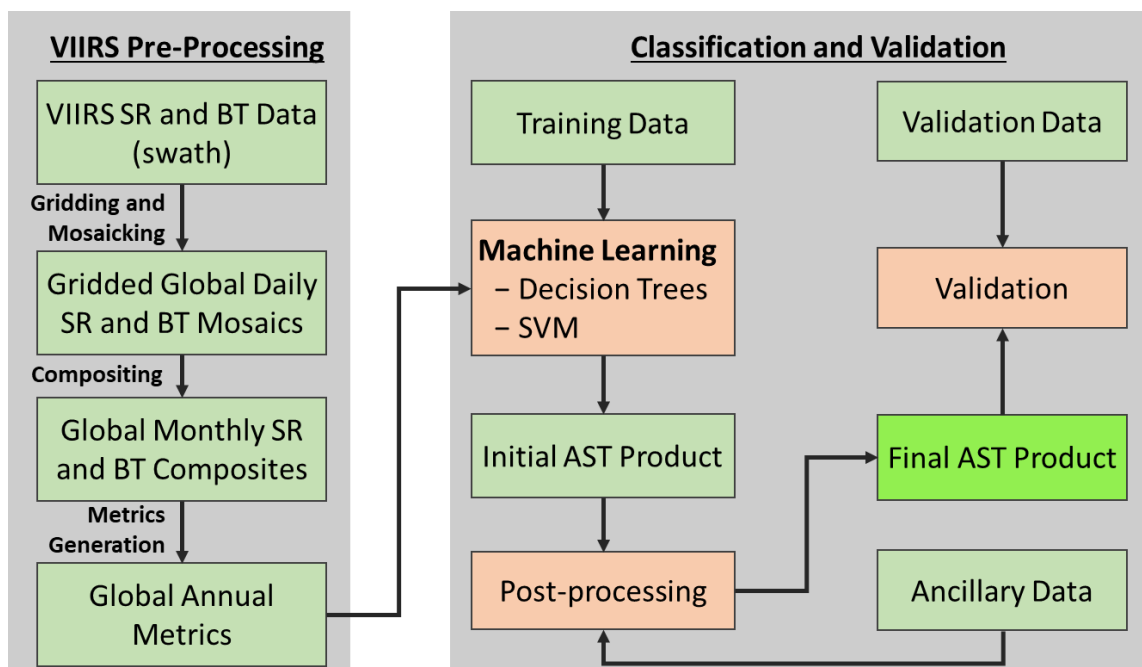
Figure 2-1. Processing flow of the VIIRS AST algorithm.

The annual metrics constitute the inputs to the second step – surface type mapping. Two advanced machine learning algorithms – decision trees (DT) and support vector machines (SVM), have been used to produce the AST products. A globally representative training

dataset is used to train these algorithms. The final AST products are produced by applying a sequence of post-processing procedures to the initial AST products generated by the machine learning algorithms to remove some known errors in those initial products.

2.2. Algorithm Input

Major inputs to the AST algorithm include VIIRS M1 – M5, M7, M8, and M10 – M16. All VIIRS observations acquired during daylight time in a year in these bands are used in producing the AST for that year. Other inputs include training data, ancillary data, and validation data.

Training data are required to train the machine learning algorithms used in the AST production. The initial AST training dataset consisted of samples included in the System for Terrestrial Ecosystem Parameterization (STEP) database (Muchoney et al. 1999). In order to be trained adequately, the machine learning algorithms require large quantities of training samples to represent the global distribution and spectral-temporal signatures of different surface types. Additional training samples have been selected from areas where existing global land cover products have high levels of agreements, which serve as indicators that those areas likely have been classified correctly by those products (Song et al. 2014a; Song et al. 2017). An in-house tool has been developed to verify those samples using high resolution images available from Google Earth. The tool plots the 1-km footprint of a sample on Google Earth. An analyst then examines the available Google Earth image to determine the surface type for that sample (Figure 2-2).

(a) Eastern Africa (14.1667°N, 35.0750°E)   (b) Southern Canada (50.4750°N, 108.6163°W)
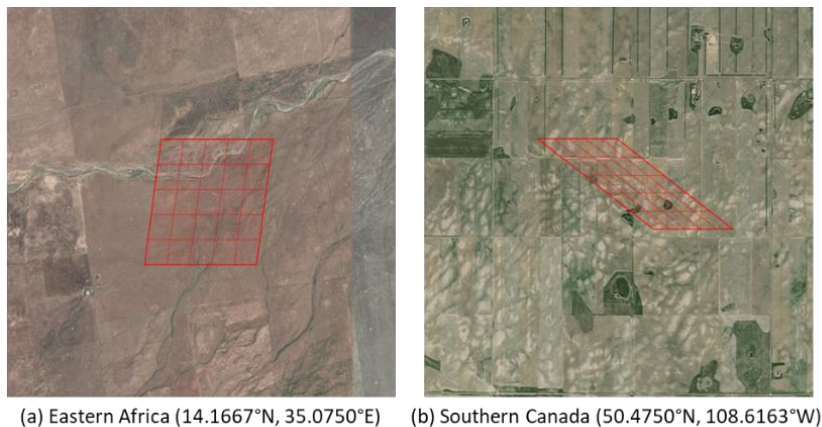
Figure 2-2. An in-house tool has been developed to facilitate labeling training and validation samples based on available high resolution Google Earth (GE) images. The tool draws the 1-km grid cell area covered by a sample over the GE image. To help interpretation, each grid cell is divided into 25 equal-sized smaller cells. The two example sites show how the 1-km grid cells in the Sinusoidal projection are distorted differently in different regions.

The number of samples in the current AST training dataset is listed in Table 2-1. Their spatial distribution is shown in Figure 2-3. It is expected that additional training samples will be added and/or corrections of existing samples be made in the future using the in-house tool shown in Figure 2-2.

Table 2-1. Number of training samples available for generating the VIIRS AST product. No training samples are selected for the urban and built-up lands (13) and water bodies classes (17) because they are mapped based on ancillary datasets.

IGBP class number	IGBP class name	Number of pixels in training
1	Evergreen needleleaf forests	1223
2	Evergreen broadleaf forests	5881
3	Deciduous needleleaf forests	558
4	Deciduous broadleaf forest	991
5	Mixed forests	1972
6	Closed shrublands	389
7	Open shrublands	6239
8	Woody savannas	2933
9	Savannas	3330
10	Grasslands	5554
11	Permanent wetlands	1439
12	Croplands	8184
13	Urban and built-up lands	0
14	Cropland/natural vegetation mosaics	1304
15	Snow and ice	859
16	Barren	4233
17	Water bodies	0
Total		45089

Ancillary datasets are mainly used during the post-processing stage. A list of these datasets is provided in Table 2-2. Their specific uses are detailed in section 2.3.2.4.
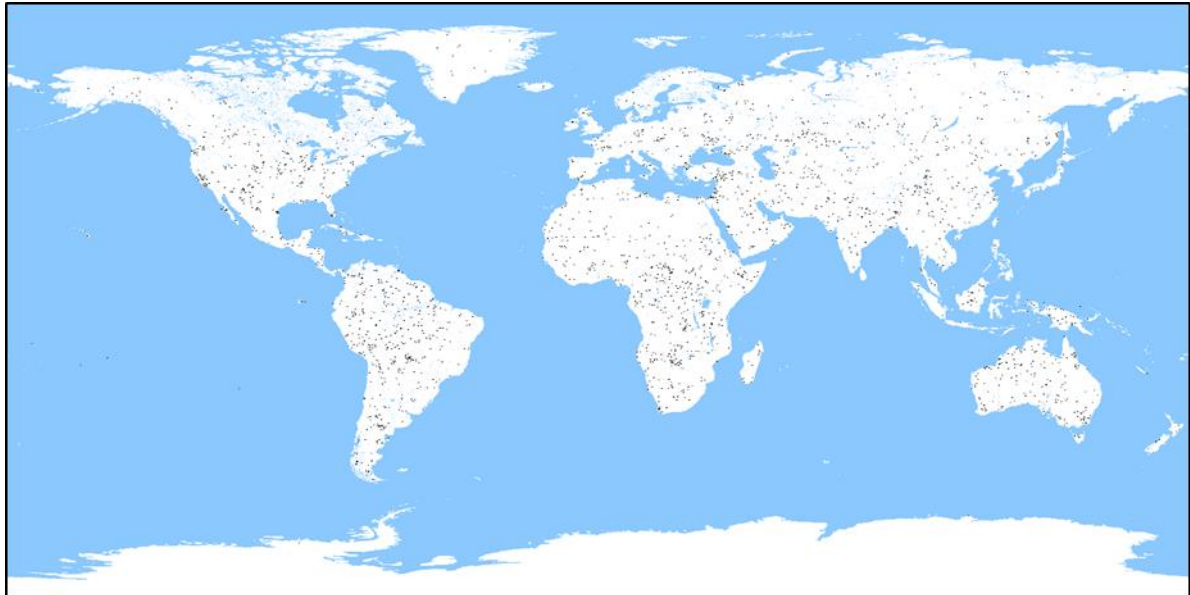
Figure 2-3. Spatial distribution of the training sites that have been collected for generating the VIIRS AST product.

Table 2-2 Ancillary datasets used in producing the VIIRS AST product.

Ancillary data source	Citations
Urban mask	Schneider et al. (2009)
Land/water mask	Carroll et al. (2009)
Ecoregion map	Olson et al. (2001)
Crop probability map	Pittman et al. (2010)
Google Map/Earth data	Google.com
Local Landsat data	

Validation of the AST product requires reference samples selected following a probability based sampling design method (Olofsson et al. 2014; Stehman and Czaplewski 1998). The AST validation samples are selected through a stratified random sampling process. The percentage allocation of the validation samples for each surface type is calculated according to Figure 1 of Olofsson et al. (2012) (Table 2-3). A total of 6000 validation samples have been selected following this strategy and labeled based on Google Earth images and other available high resolution data sources using the in-house tool shown in Figure 2-2. The spatial distribution of these samples is shown in Figure 2-4.

Table 2-3. Reference samples that have been collected for validating the VIIRS AST product. The samples for the water bodies class are selected from inland water bodies.

Class number	Class name	Number of validation samples	Percentage in the validation dataset (%)
1	Evergreen needleleaf forests	240	4
2	Evergreen broadleaf forests	600	10
3	Deciduous needleleaf forests	120	2
4	Deciduous broadleaf forest	180	3
5	Mixed forests	360	6
6	Closed shrublands	60	1
7	Open shrublands	660	11
8	Woody savannas	660	11
9	Savannas	300	5
10	Grasslands	720	12
11	Permanent wetlands	60	1
12	Croplands	960	16
13	Urban and built-up lands	120	2
14	Cropland/natural vegetation mosaics	540	9
15	Snow and ice	60	1
16	Barren	300	5
17	Water bodies	60	1
Total		6000	100

2.3. Theoretical Description

2.3.1. Physical Description

Satellite data have been used to map land cover for nearly half a century. The fact that many surface types have different spectral signatures (Figure 2-5) provide a strong physical basis for such practices. For global observing systems like VIIRS, MODIS, and AVHRR, although such spectral differences may not be as distinctive as they should be because most pixels at the quasi-km spatial resolutions of these instruments are highly mixed, their daily observing capabilities make it possible to capture the full annual phenological dynamics across the globe. Following an early study by DeFries and Townshend (1994) demonstrating the value of phenological information for global land cover mapping, such information has become a key component in developing global land cover products from MODIS, AVHRR, and other quasi-km resolution global observing systems (Bartholome and Belward 2005; Friedl et al. 2010; Friedl et al. 2002; Hansen et al. 2000; Loveland et al. 2000).
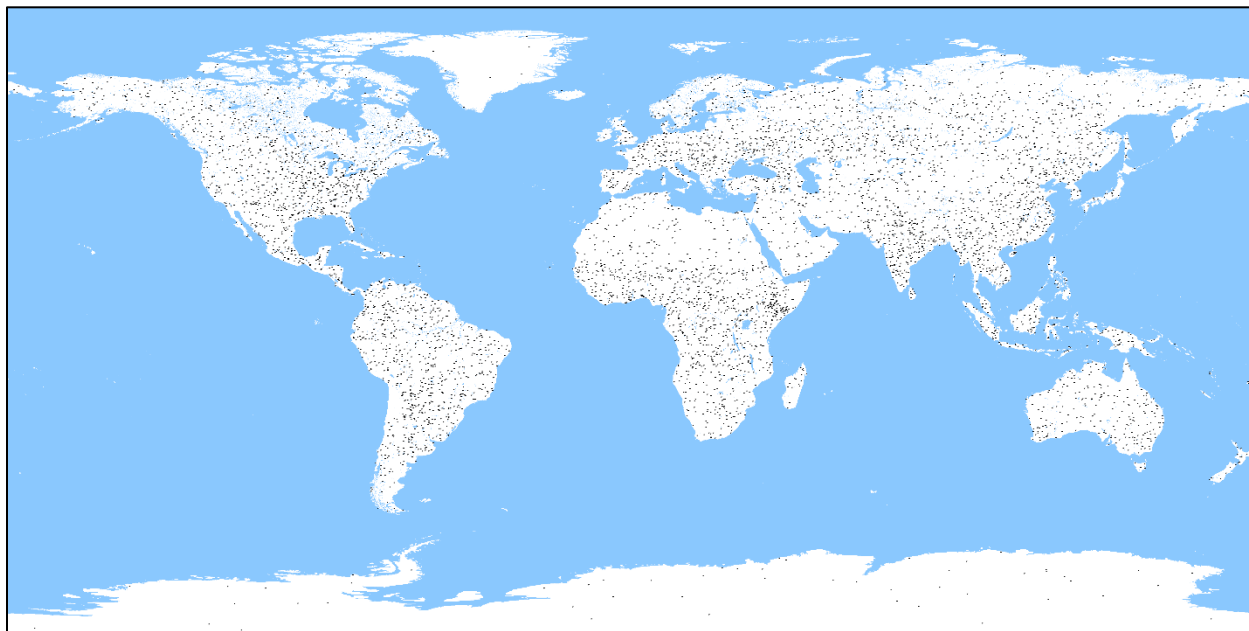
Figure 2-4. Spatial distribution of the reference samples that have been collected for validating the VIIRS AST product.

.
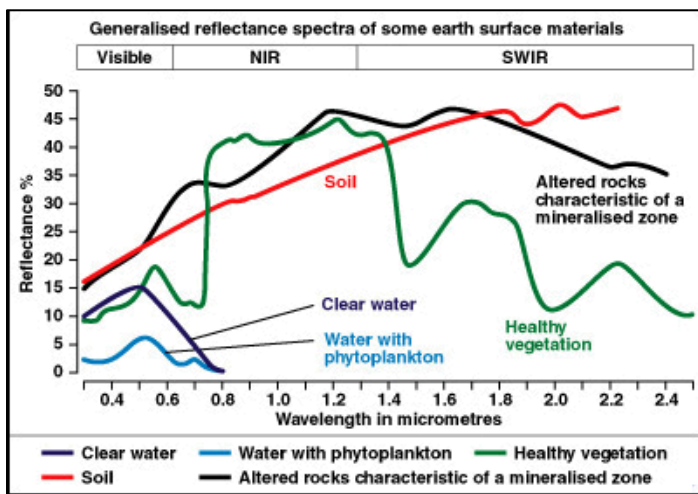
Figure 2-5. Laboratory measured spectra for selected surface cover types (Based on spectral data from https://speclab.cr.usgs.gov/spectral.lib06/ds231/index.html).

Due to frequent cloud and shadow presence in many regions, many observations acquired in any given date are obscured or contaminated by clouds/shadow (e.g., see Figure 2-6 in section 2.3.2.1). Use of such observations in surface type mapping most likely will produce

erroneous results, as such observations provide little or no information over the concerned surface area. Compositing is a common practice for creating cloud free or near cloud free datasets. The physical basis of such compositing algorithms is that the spectral-temporal signatures of cloud and shadow are often different from those of clear view surface areas (Holben 1986).

Once cloud free global datasets have been created, machine learning algorithms are often used to classify these datasets to produce surface type products. Although other methods have been used to produce global land cover products (e.g. Loveland et al. 2000), given adequately representative training datasets, a machine learning approach is more objective, repeatable, and often produces more accurate results (Huang et al. 2003). In fact, most existing global land cover products are produced using machine learning algorithms (Friedl et al. 2010; Friedl et al. 2002; Hansen et al. 2000; Zhang et al. 2016; Zhang et al. 2017).

2.3.2. Mathematical Description

This section provides a detailed description of the algorithms and procedures needed for producing the VIIRS AST product (Figure 2-1).

2.3.2.1 Gridding and Compositing

Global land cover mapping algorithms require gridded satellite data, but for VIIRS such data are not available from existing operational processing systems. Therefore, the AST team developed an in-house algorithm based on the MODIS heritage gridding algorithm for mapping swath level VIIRS data into the Sinusoidal grid space. All VIIRS swath data acquired during the daylight time of each day are gridded and used to create a global mosaic for that day. As shown in Figure 2-6, these daily mosaics typically have substantial clouds in many areas across the globe.

Compositing is a commonly used procedure for reducing clouds in global datasets. Given the fact that clouds are often brighter and hence have lower NDVI values than many clear view surfaces, compositing methods that use a single criterion (e.g., max NDVI, minimum blue) are common (e.g. Chuvieco et al. 2005a; Holben 1986). A major limitation of such single criterion methods is that they are optimized for certain surface cover conditions but not for others. For example, cloud presence over barren or vegetated surfaces typically results in lower NDVI values. For such surfaces, a clear view observation can be selected using a MaxNDVI method that chooses the observation having the highest NDVI value (Holben 1986). However, this method does not work for water and snow/ice, because water has lower NDVI values than clouds, and snow/ice may also have lower NDVI values than clouds. But both water and snow/ice have much lower values in the M10 band (1.61 µm)

than clouds. A minimum M10 method would be more effective for selecting clear view observations for surfaces covered by water or snow/ice. This compositing method is referred to as MinSWIR2, because the 1.61 µm band is often referred to as the second shortwave infrared (SWIR2) band in land applications.
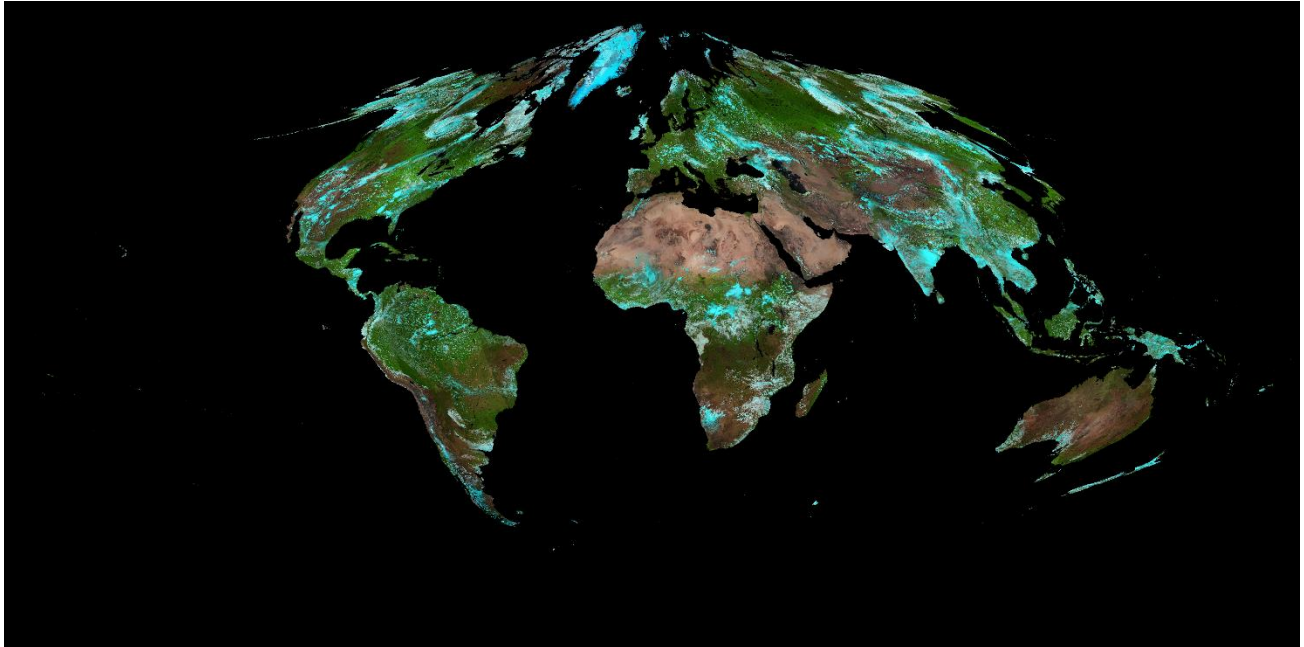
Figure 2-6. A global mosaic of VIIRS observations acquired on July 15, 2018 in the Sinusoidal projection. Many areas of the globe have cloud cover in such daily mosaics.

Use of multiple criteria can address some of the limitations of the single criterion methods, but existing multi-criteria methods typically require proper masking of clouds (e.g. Chuvieco et al. 2005b; Frantz et al. 2017; Griffiths et al. 2013; Luo et al. 2008; Roy et al. 2010). Unfortunately, VIIRS did not have a reliable cloud mask product for use by the AST algorithm during early stages of the S-NPP mission. To address this issue, the AST team developed a self-adaptive compositing (SA-Comp) algorithm that does not require a cloud mask product (Bian et al. 2018). In this approach, different compositing criteria are used to select clear view observations for different surface cover condition (SCC). As discussed earlier, the MaxNDVI method works well for both barren and vegetated surfaces, but when the surface is covered by water or snow/ice, the MinSWIR2 method is needed (Figure 2-7).

SA-Comp uses the following rules to determine whether the surface is barren or is covered by vegetation, water, or snow/ice (Figure 2-7):
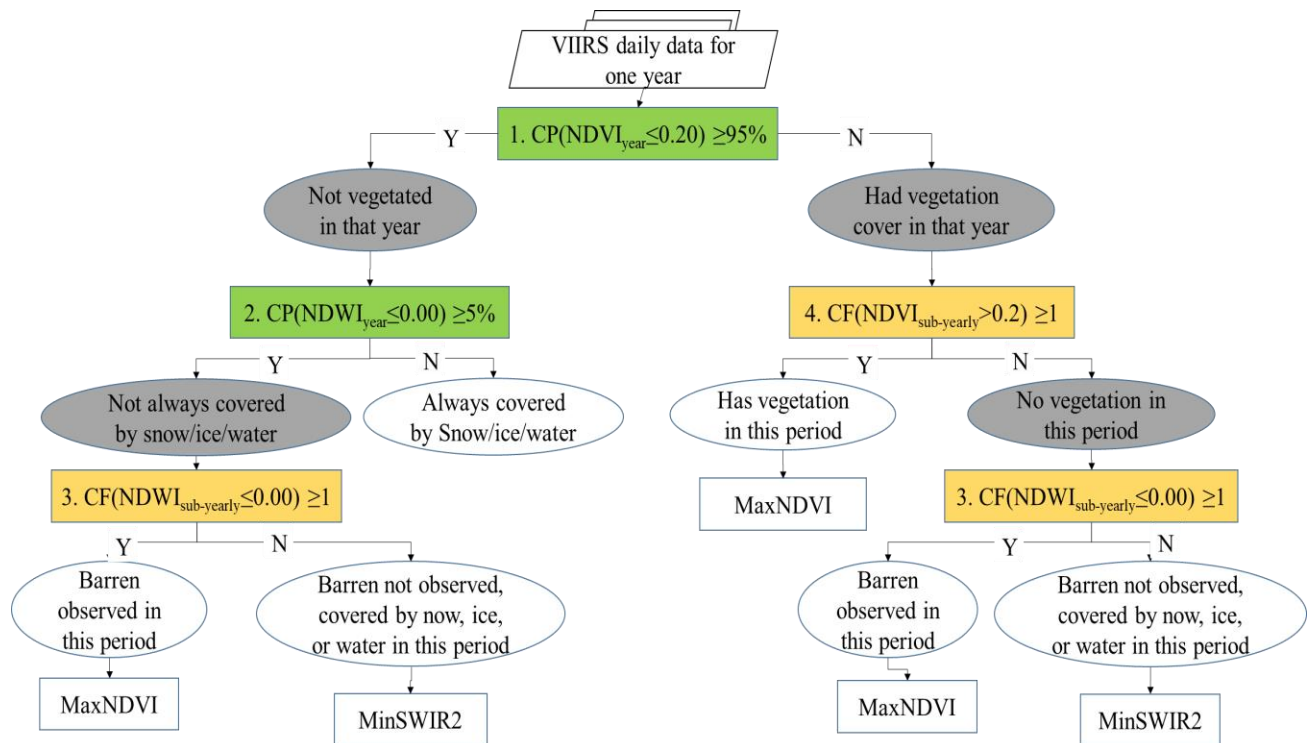
Figure 2-7. A flowchart of the decision rules and compositing criteria used in the SA-Comp method. CP is the cumulative percentage of observations in a year that meet the conditional statement in the parentheses, whereas CF is the cumulative frequency within a specific compositing period.

Rule 1: If more than 95% of a pixel's daily observations in a year had NDVI values below 0.2, the pixel was not vegetated throughout the year and will be evaluated using Rule 2. Otherwise it had vegetation cover during at least part of the year and will be evaluated using Rule 4.

Rule 2: For a pixel that had no vegetation cover during the entire year, it was covered by snow/ice or water throughout the year if its NDWI values were negative for less than 5% of the time. The MinSWIR2 criterion is used for all compositing periods of the year. Otherwise barren was observed during at least part of the year, and whether barren was observed during a specific compositing period needs to be determined using Rule 3.

Rule 3: Since the pixel was not vegetated throughout the year and hence not vegetated during a specific compositing period, and barren was observed during at least part of a year, barren was observed during a compositing period if at least one daily observation in this period had a negative NDWI value, and the MaxNDVI criterion is used for this compositing period. Otherwise barren was not observed, meaning

the pixel had snow/ice or water cover during the entire compositing period, and hence the MinSWIR2 criterion is used.

Rule 4: Since the pixel had vegetation cover during at least part of the year according to Rule 1, it had vegetation cover in a specific period if at least one daily observation in this period had an NDVI value > 0.2, and the MaxNDVI criterion is used. Otherwise it did not have vegetation cover during this period, and Rule 3 is used to determine whether barren was observed during this period.

The SA-Comp method significantly improves upon existing single-criterion methods with regard to the discrimination of clouds and cloud shadows (Figure 2-8). It also produces data that are better than standard MODIS composites as well as an early version of VIIRS composites produced using a MODIS heritage compositing method (Figure 2-9).
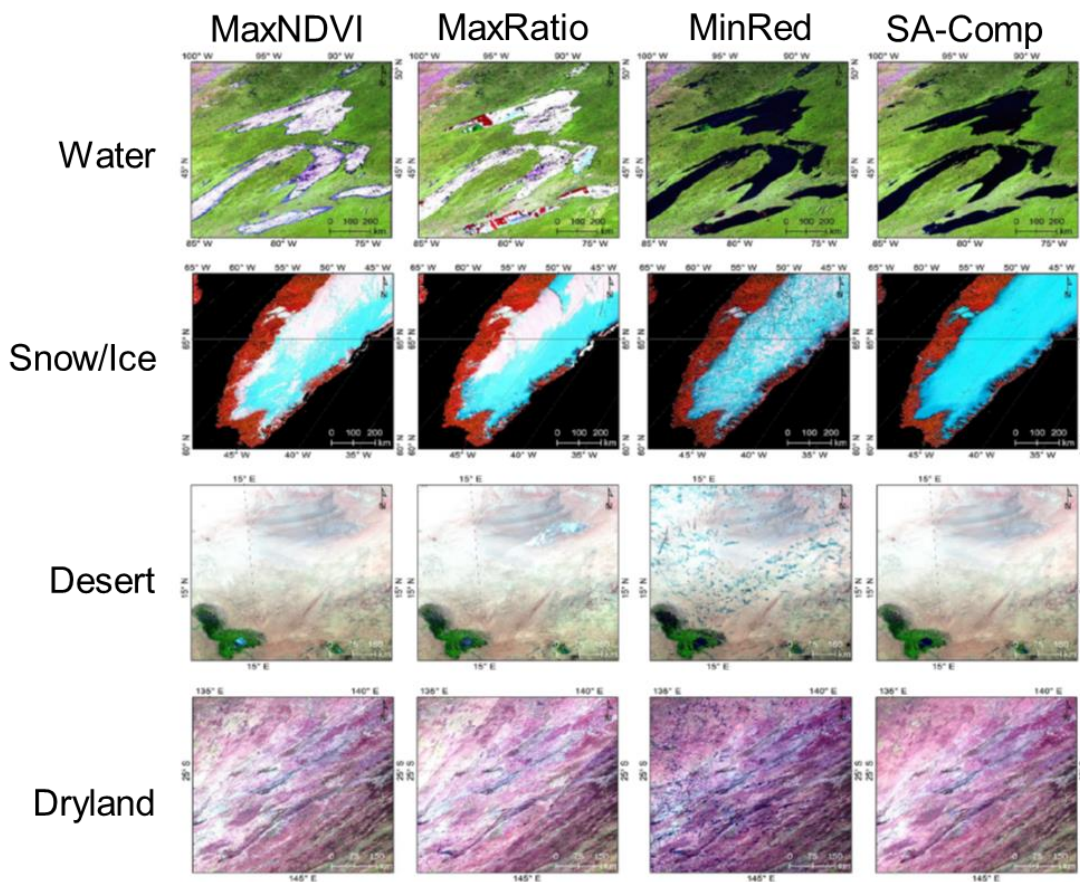
Figure 2-8. A comparison of VIIRS 16-day composites generated by three single-criterion methods and the SA-Comp method showing that while each single-criterion method may work well for certain surface cover conditions but not for others, the SA-Comp method works well for all conditions.
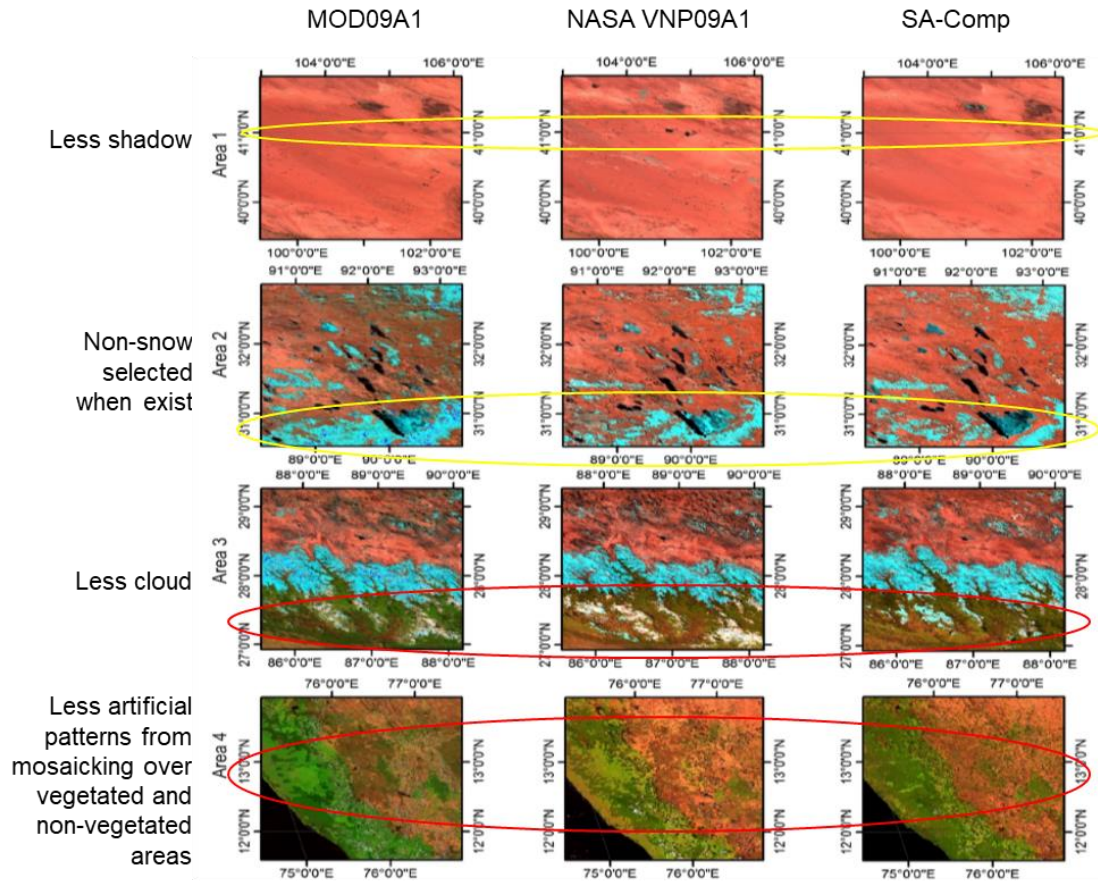
Figure 2-9. Advantages of the SA-Comp method illustrated through a comparison of VIIRS 8-day composites generated using this method with the MODIS MYD09A1 (8-day) and an early version of NASA VNP09A1 8-day surface reflectance products produced using a MODIS heritage compositing method.

2.3.2.2 Metrics Generation

One of the challenges to surface type discrimination at the global scale is that the spectral-temporal signature of each surface type can vary greatly depending on geographic location. It has been demonstrated that temporal metrics such as annual maximum, minimum and mean values can greatly reduce the geographic variability of the spectral-temporal signature of surface types (DeFries et al. 1999; Hansen et al. 2000; Hansen et al. 2003). Such metrics are typically derived from observations acquired over one full calendar year (Friedl et al. 2010; Friedl et al. 2002; Loveland et al. 2000).

Following methods that have been successfully used to develop global land cover and continuous fields products from MODIS and AVHRR (DeFries et al. 1999; Hansen et al. 2000; Hansen et al. 2003; Hansen et al. 2002; Hansen et al. 2005), the following temporal metrics are used in developing the VIIRS AST product (Table 2-4):

- The maximum, minimum, mean and amplitude values calculated using the monthly composites of the 8 greenest months of the past 12 months. Here use of the 8 greenest months instead of all 12 months of a calendar year effectively reduces the complications caused by seasonal snow covers and yet retains the seasonal variability associated with vegetation phenology. The 8 greenest months are not necessarily consecutive, but represent the 8 months with the clearest view of green vegetation.
- Observations acquired in the greenest month selected by choosing the highest monthly NDVI value
- Observations acquired in the warmest month selected by choosing highest monthly M14 brightness temperature.
- Mean value of the warmest 4 months, where the warmest 4 months have the highest monthly M14 brightness temperature. This set of metrics were found to be associated with the dry season or senescent phase of tropical vegetation. It provides information useful for some areas but is not included in the 8 greenest months without introducing snow values at elevations or over high latitude regions (Hansen et al. 2000).

Table 2-4 Annual metrics used in the VIIRS AST algorithm, where x refers to VIIRS bands M1, M2, M3, M4, M5, M7, M8, M10, M11, and M14.

Maximum NDVI value
Minimum NDVI value of 8 greenest months
Mean NDVI value of 8 greenest months
Amplitude of NDVI over 8 greenest months
Mean NDVI value of 4 warmest months
NDVI value of warmest month
Maximum band x value of 8 greenest months.
Minimum band x value of 8 greenest months.
Mean band x value of 8 greenest months.
Amplitude of band x value over 8 greenest months.
Band x value from month of maximum NDVI.
Mean band x value of 4 warmest months.
Band x value of warmest month.

2.3.2.3 Machine Learning Algorithms

The annual metrics generated in section 2.3.2.2 are classified using advanced machine learning algorithms. A modified C4.5 decision tree algorithm was used to produce global land cover maps from MODIS (Friedl et al. 2010; Friedl et al. 2002). For VIIRS, a newer version of C4.5, C5, was used to produce the AST for 2012 following the pre-launch ATBD for Surface Type EDR. However, studies conducted over the last decade or so have reached a consensus that the support vector machines (SVM) typically produces more accurate classifications that are also spatially more coherent (e.g., less "salt and peppers"). Therefore, SVM has been selected for generating VIIRS AST for 2014 and later years. A brief description of both the C5 and SVM is provided below.

Decision Tree – C5

C5 is one of the most widely used commercial decision tree algorithms for land cover classification and many other applications. While the algorithm details of this software are unknown due to its proprietary nature [2], some details on its predecessor – C4.5, have been published (Quinlan 1993). The following summary of the C4.5 algorithm is based on Quinlan (1993), and is provided to illustrate the general algorithm concept of the C5 software.

The C4.5 decision tree algorithm employs a gain ratio method to partition training samples into subsets, i.e., during the recursive partitioning process, each partitioning X is made to maximize a Gain_Ratio measure:

$$Gain\_Ratio(X) = Gain(X) / Split\_Info(X)$$

Where gain(X) is a measure of the information gained by partitioning a set T of $|T|$ cases into n subsets ($T_1, \cdots, T_n$):

$$Gain(X) = Info(T) - Info_X(T)$$

Suppose there are k classes in set T, and the number of cases of the jth class in T is C_j, then

---

[2] See https://www.rulequest.com/see5-info.html for general information about the C5 software package.

$$Info(T) = -\sum_{j=1}^{k} \frac{C_j}{|T|} \times \log_2\left(\frac{C_j}{|T|}\right)$$

and

$$Info_X(T) = -\sum_{i=1}^{n} \frac{|T_i|}{|T|} \times Info(T_i)$$

Split_Info(X) is defined by analogy with the definition of Info(T):

$$Split\_Info(X) = -\sum_{i=1}^{n} \frac{|T_i|}{|T|} \times \log_2\left(\frac{|T_i|}{|T|}\right)$$

Using the Gain_Ratio instead of the Gain as the splitting criterion avoids near trivial splits that produce high accuracy on training data but generalize poorly over unseen samples (Quinlan 1993).

One of the advanced features of the C5 program is boosting. Boosting is an ensemble technique designed to improve the accuracies of weak classifiers, the effectiveness of which has been demonstrated in many studies (Bauer and Kohavi 1998; Chan et al. 2001; Chan and Paelinckx 2008; Friedl et al. 1999). It can also reduce the "salt and pepper" phenomenon common to remote sensing derived land cover products (Homer et al. 2004; Huang et al. 2003). When the boosting feature is used, the C5 algorithm builds a sequence of trees, where each tree is constructed to correct errors of the previous tree. Each pixel is classified by all trees constructed through the boosting process, and the final class label of that pixel is a weighted voting of the classification results derived by all trees over that pixel. Bauer and Kohavi (1998) provided a detailed mathematical description of the boosting algorithm.

Support Vector Machines (SVM)

The mathematical formulation of the SVM has been detailed in many publications (e.g. Burges 1998; Huang et al. 2002; Huang and Song 2012; Vapnik 1995). A brief summary is provided below following these publications.

The inductive principle behind SVM is structural risk minimization (SRM) designed to minimize overfitting, a problem common to classification models developed using neural networks and decision trees (Foody and Arora 1997; Friedl et al. 1999; Paola and Schowengerdt 1995). According to Vapnik (1995), the risk of a learning machine (R) is

bounded by the sum of the empirical risk estimated from training samples (R_{emp}) and a confidence interval (Ψ):

$$R \leq R_{emp} + \Psi$$

The strategy of SRM is to keep the empirical risk (R_{emp}) fixed and minimize the confidence interval (Ψ). This is achieved by maximizing the margin between a classification boundary and the support vectors, i.e., training samples closest to the classification boundary. This optimization problem can be solved mathematically for linear classification boundaries. The actual boundaries between different surface types, however, are rarely linear. Kernel functions are used to extend this algorithm concept to nonlinear boundaries, which can greatly improve classification accuracy (Figure 2-10). One of the most robust kernel functions widely used in land cover classification is the radial basis function (RBF):

$$K(x_1, x_2) = e^{-\gamma(x_1 - x_2)^2}$$

The SVM algorithm has been implemented in several computer packages. The πSVM [3] – a parallel SVM software built on the LibSVM package and Message Passing Interface (MPI) framework, is selected for AST production. The LibSVM [4] software package is publicly available. It has been widely used in land cover studies (Mountrakis et al. 2011). The parallel implementation greatly reduces the amount of time needed to produce the AST product.

| Linear boundary | gamma=1 | gamma=0.5 | gamma=0.2 | gamma=0.1 |
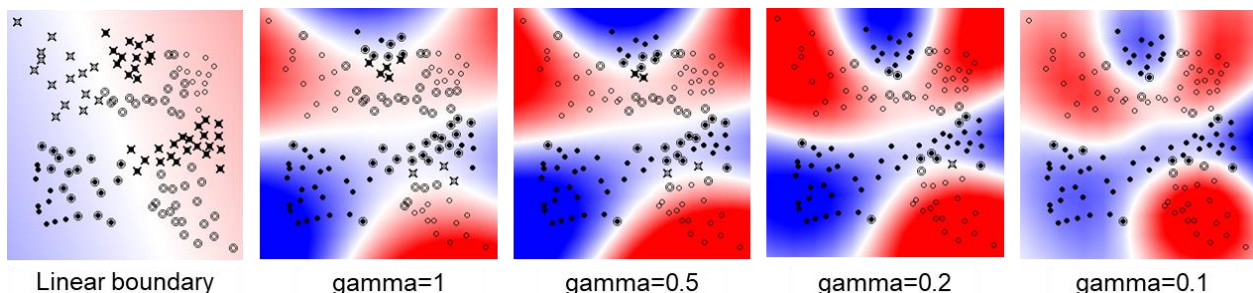
Figure 2-10. Use of linear decision boundaries to classify data having nonlinear boundaries can result in large misclassification errors (left most). The class boundaries can be better represented using the RBF kernel with progressively fine-tuned gamma values, which can result in minimum or no classification errors (from the 2nd to the 5th). Samples of the two classes are represented by empty and solid circles. Circled points are support vectors, and checked points are misclassification errors. Created based on Huang et al. (2002).

---

[3] See http://pisvm.sourceforge.net/ for general information about the πSVM package.

[4] See https://www.csie.ntu.edu.tw/~cjlin/libsvm/ for details about the LibSVM package.

2.3.2.4 Post-Processing

There are two goals for post-processing. The first is to incorporate two classes – built-up lands and water bodies, into the initial AST product generated by the machine learning algorithms. These two classes are not included in the initial classification, which is a common practice in previous global land cover mapping efforts (Friedl et al. 2010; Friedl et al. 2002; Hansen et al. 2000). Two existing products are used to define these two classes, including a MODIS based global urban area map developed by Schneider et al. (2010), and a global water mask dataset developed by Carroll et al. (2009).

The second post-processing goal is to correct for some of the errors in the initial AST product. For example, confusions between croplands, cropland/natural vegetation mosaic, grasslands, and open shrublands exist in many areas. This is partly due to a lack of clear boundaries between some of these classes and partly because pixels of these classes are often highly mixed. Posterior classification probabilities and ancillary data layers are used to reduce some of these errors. Some of the ancillary datasets useful for post-processing are listed in Table 2-2.

2.4. Algorithm Output

The primary output of the above described processing flow is the final AST map produced using VIIRS observations acquired within a year. Figure 2-11 shows the 2014 AST map reprojected using the geographic projection.

To facilitate broad use of the VIIRS AST product, two variations of this product are produced. The first consists of the biome classes required by a leaf area index (LAI) algorithm (Myneni et al. 1997). The other is a 20-class map for use by the National Centers for Environmental Prediction (NCEP) land team in land surface models.
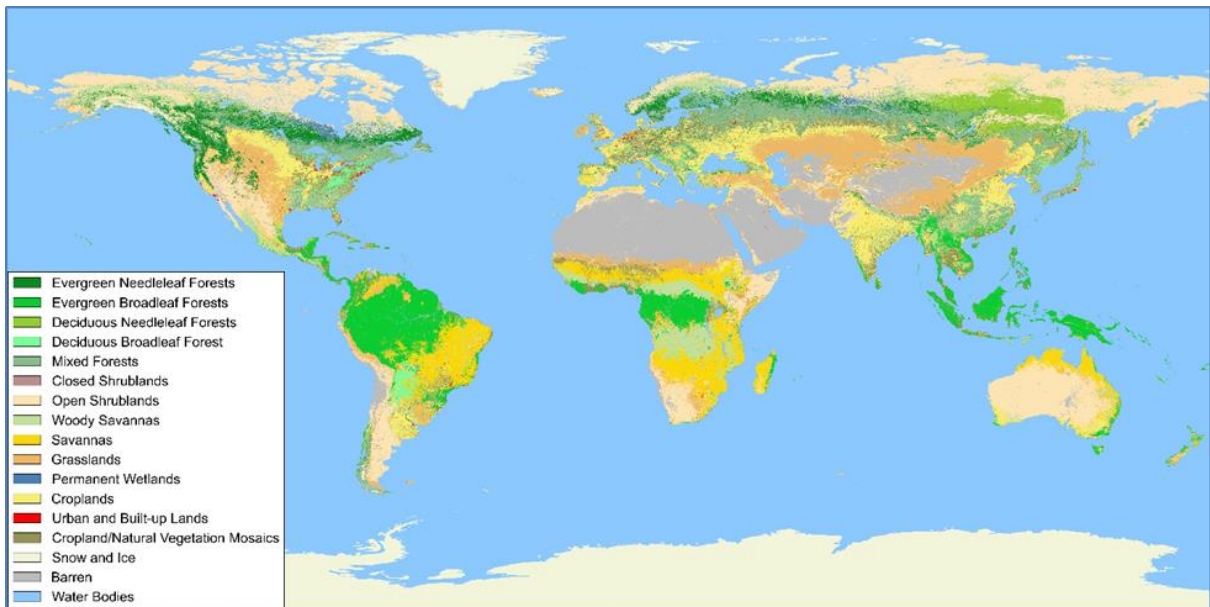
Figure 2-11. Final AST map based on 2014 VIIRS observations in the geographic projection.

Biome Map

The biome map includes 6 biome classes for vegetated areas and 3 classes for non-vegetated areas:

0. Water
1. Grasses and Cereal Crops
2. Shrubs
3. Broadleaf Crops
4. Savannas
5. Broadleaf Forests
6. Needleleaf Forests
7. Unvegetated
8. Urban

This product is generated based on the 17-class AST map and ancillary datasets using a look-up-table (LUT, Figure 2-12). The following ancillary datasets are used by the LUT:

- Second classification label of the SVM classification
- The World Wildlife Fund (WWF) biome map, and
- An agriculture type (ag_type) map

```
IGBP = 17, BIOME = 0;
IGBP = 1, BIOME = 6;
IGBP = 2, BIOME = 5;
IGBP = 3, BIOME = 6;
IGBP = 4, BIOME = 5;
IGBP = 5, second label = 1 or 3, BIOME = 6;
IGBP = 5, second label = 2 or 4, BIOME = 5;
IGBP = 5, second label != 1, 2, 3, or 4, WWF biome = 1, 2, 4, BIOME = 5; else BIOME =
6;
IGBP = 6, BIOME = 2;
IGBP = 7, BIOME = 2;
IGBP = 8, BIOME = 4;
IGBP = 9, BIOME = 4;
IGBP = 10, BIOME =1;
IGBP = 11, second label !=11, treat second label as IGBP label and redo; else
BIOME=9
IGBP = 12, ag_type classification = 1, BIOME = 1; else BIOME = 3;
IGBP = 13, BIOME = 8;
IGBP = 14, ag_type classification = 1, BIOME = 1; else BIOME = 3;
IGBP = 15, BIOME = 7;
IGBP = 16, BIOME = 7;
```

Figure 2-12. Look-up-table (LUT) for converting the 17-class AST product to a biome map required by the LAI algorithm of Myneni et al. (1997).

The ag_type map is produced based on training data provided by the STEP database (Muchoney et al. 1999). The biome map derived using the 2014 AST product is shown in Figure 2-13.

20-Class Map for NCEP Models

In addition to the 17-IGBP types, NECP land surface models require that the tundra region be classified into three classes: wooded tundra, mixed tundra, and bare ground tundra. These three tundra types are derived based on the MODIS global land cover product and other ancillary data. The 20-class map derived using the 2014 AST product is shown in Figure 2-14.
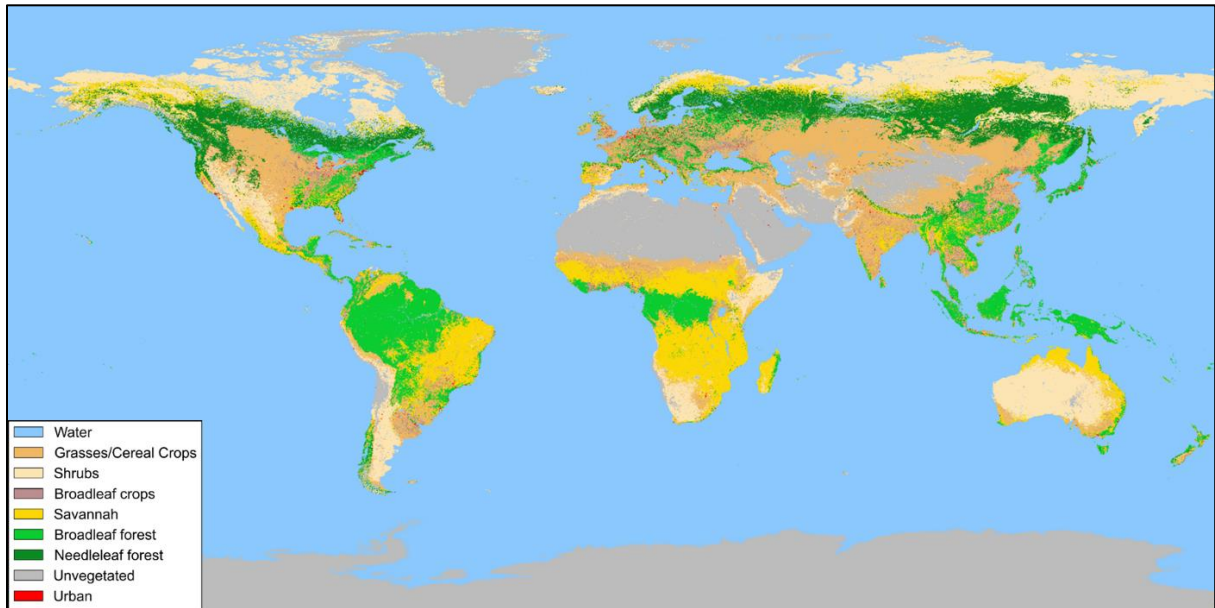
Figure 2-13. Biome type map derived based on the 2014 AST product for use by the LAI algorithm of Myneni et al. (1997).
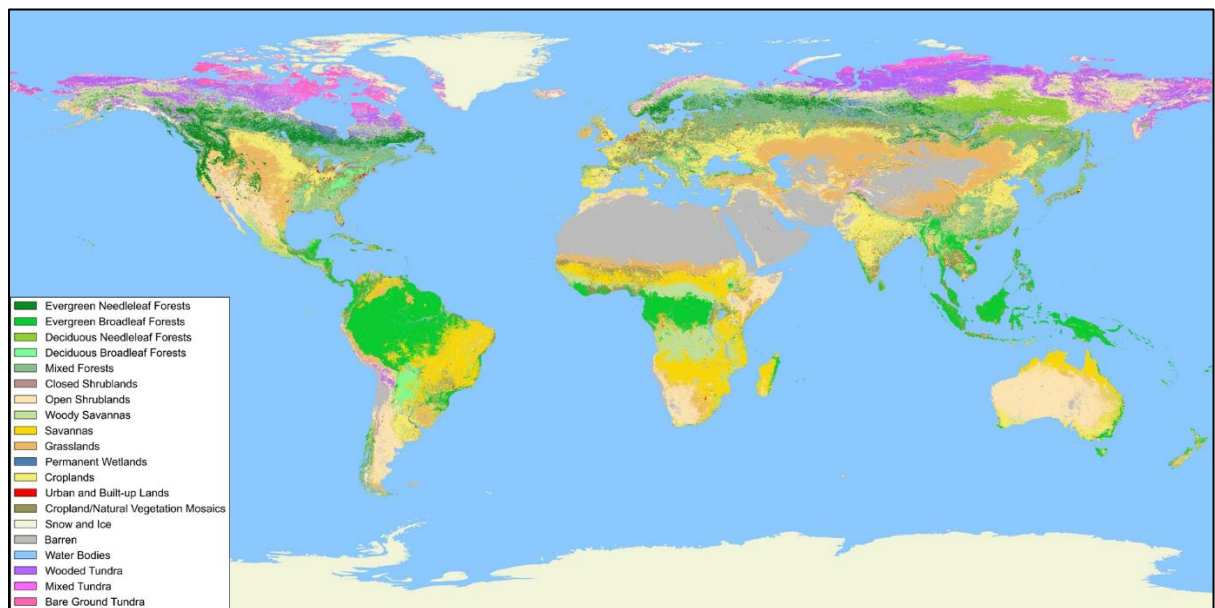
Figure 2-14. The 20-class map derived based on the 2014 AST product for use by NCEP land surface models.

2.5. Performance Estimates

2.5.1. Test Data Description

Test data for evaluating the AST product has been described in section 2.2

2.5.2. Sensor Effects

The AST algorithm might be affected by large geometric and/or radiometric errors in VIIRS data. However, both the geometric correction and radiometric calibration of the VIIRS data are adequately accurate for the AST algorithm. Clouds, shadows, and other bad observations, if not flagged or filtered, tend to produce erroneous results. Most of such bad observations should have been removed through compositing and metrics generation described in sections 2.3.2.1-2.3.2.2. For extremely cloudy regions, however, some of the composites and metrics may still be contaminated by clouds or shadows. Although it is hard to estimate the number of pixels subject to such residual noises, their fractions should be extremely small (<< 1%).

2.5.3. Retrieval Errors

Both the C5 and SVM algorithms can produce highly accurate results if the training samples provided are representative, the classes are separable, and the input data (including both the predictor variables, i.e., annual metrics, and the training data) are immune from noises. In reality, however, it is impossible to provide a training dataset that is error free and can adequately represent the spectral-temporal signatures of different surface types distributed in different regions of the globe. This is exacerbated by the fact that because transitions between some of the surface types are a continuum in many regions, clear boundaries between them may not exist. Further, the annual metrics to be classified by the machine learning algorithms are not error free. As discussed in section 2.5.2, in extremely cloudy regions, some pixels may still be contaminated by cloud/shadow.

It is extremely difficult, if not impossible, to quantify the magnitude of each of these error sources, and hence the difficulty to estimate the error budget arising from each factor. The accuracy assessment results reported in section 2.7 reflect the aggregated errors of all these factors. Overall, these errors in each of the AST products generated thus far do not exceed the error level specified in Table 1-1 (see detailed discussions in section 2.7).

2.6. Practical Considerations

2.6.1. Numerical Computation Considerations

Development of the AST is both CPU and storage intensive. It requires processing of all VIIRS observations in the selected bands acquired during daylight time over a full calendar year. The total volume of all data files required or generated by this process exceeds 100 TB. Most of the preprocessing procedures, including gridding, mosaicking, and compositing, need to be performed monthly or more frequently. To reduce storage needs to a manageable level, the swath level raw data are removed after being gridded.

Use of the machine learning algorithms to produce the AST product is both CPU and I/O intensive. Some level of parallel processing is needed to improve processing efficiency. This is achieved in two ways. One is to divide the globe into smaller tiles (e.g., the standard tiling system used by MODIS products) and process different tiles in parallel. The other is to use a parallel version of the SVM – πSVM, to produce the AST.

2.6.2. Programming and Procedural Considerations

The AST is an offline product to be generated by the surface type team outside any operational VIIRS processing systems (e.g., IDPS, NDE). This is appropriate because the AST does not need to be generated on a daily or near real time basis, which is what the IDPS and NDE are designed to achieve. Many key procedures of the AST algorithm, including training data development, post-processing, and accuracy assessment, require frequent user inputs, which is difficult for an operational system to accommodate. On the other hand, the high processing efficiencies operational systems aim to provide are not as critical to these procedures as to those needed to produce some other VIIRS products.

That said, the AST algorithm can leverage the processing capabilities of an operational processing system like the NDE. In particular, downloading the swath level data is one of the most time consuming parts of the current implementation of the gridding and mosaicking process for generating gridded global daily SR and BT mosaics from swath level observations. The time and storage needs incurred by this step could be completely eliminated if it could be implemented on an operational processing system like the NDE.

2.6.3. Quality Assessment and Diagnostics

Quality assessment is achieved through both visual assessments and accuracy assessment. Visual assessment provides an effective method for diagnosing many issues that may arise throughout the AST processing flow. Missing granules, residual clouds in the monthly composites, and/or large initial misclassification errors are among some of the issues encountered in producing an AST product. They can be identified through visual

assessments of the daily mosaics, monthly composites, annual metrics, and the initial AST product generated by the machine learning algorithms. Timely identification of these issues is critical for addressing them and preventing errors that may be caused by them propagating to the final AST product.

Once the final AST is produced, the final assessment of the product is achieved through validation and accuracy assessment, which is described in section 2.7.

2.6.4. Exception Handling

This AST will be produced for all land surfaces, including inland water bodies.

2.7. Validation

The AST product is validated following a rigorous design-based accuracy assessment procedure. The reference samples required for such an assessment have been described in section 2.2. These samples are used to create an error matrix and calculate accuracy estimates following established methods (Olofsson et al. 2014; Stehman 1999; Stehman and Czaplewski 1998). The error matrices for the 2012 and 2014 AST products are shown in Tables 2-5 and 2-6. Both products have accuracies around 78%, which exceed the 70% requirement listed in Table 2-1.

Table 2-5. Error matrix derived through accuracy assessment of the 2012 AST product. The surface types are numbered the same way as shown in Table 1-2.

Classification	Reference																Total (%)	User's accuracy (%)	Producer's accuracy (%)
	1	2	3	4	5	6	7	8	9	10	11	12	13	14	15	16			
1	1.55	0	0.04	0.03	0.32	0	0.01	0.21	0.04	0.01	0.01	0.01	0	0	0	0	2.24	69.12 ± 3.24	79.32 ± 3.97
2	0	8.70	0	0.08	0.19	0	0	0.45	0.19	0	0	0.02	0	0.06	0	0	9.68	89.88 ± 1.33	95.06 ± 0.99
3	0.05	0	0.96	0	0.09	0.01	0	0.12	0.01	0	0	0	0	0	0	0	1.24	77.08 ± 4.31	65.02 ± 5.17
4	0	0	0.01	0.63	0.04	0	0	0.06	0.05	0.01	0	0	0	0.02	0	0	0.81	77.33 ± 3.43	27.86 ± 2.96
5	0.16	0.06	0.37	0.96	3.64	0	0	0.73	0.12	0.04	0	0.02	0.02	0.16	0	0	6.28	57.93 ± 2.81	73.63 ± 2.90
6	0	0	0	0	0	0.05	0.01	0	0	0	0	0	0	0	0	0	0.06	74.19 ± 4.56	4.43 ± 0.91
7	0.06	0	0	0.03	0.12	0.52	12.38	0.15	0.09	1.69	0.12	0.40	0.03	0.28	0	0.74	16.64	74.44 ± 1.88	89.29 ± 1.26
8	0.08	0.18	0.08	0.31	0.28	0.10	0.10	5.80	0.91	0.13	0.02	0.16	0.03	0.49	0	0	8.65	67.04 ± 2.04	63.16 ± 2.32
9	0	0.10	0	0.03	0.07	0.17	0.24	0.93	5.88	0.28	0	0.17	0.03	0.48	0	0	8.39	70.08 ± 2.94	70.38 ± 2.47
10	0.02	0	0	0.06	0.05	0.17	0.75	0.20	0.32	6.08	0	0.69	0.03	0.21	0	0.23	8.78	69.23 ± 1.91	66.36 ± 2.38
11	0.02	0	0	0.02	0.09	0	0.09	0.04	0.09	0.04	0.74	0.02	0	0	0	0	1.15	64.15 ± 6.65	81.34 ± 6.75
12	0.01	0	0.01	0.04	0.02	0.01	0.05	0.05	0.18	0.49	0.02	6.02	0.08	0.61	0	0	7.59	79.37 ± 1.44	75.78 ± 2.01
13	0	0	0	0	0	0	0	0.01	0	0	0	0.04	0.34	0.02	0	0	0.43	79.21 ± 4.06	57.26 ± 7.19
14	0	0.11	0.01	0.07	0.05	0.01	0.09	0.43	0.47	0.23	0	0.33	0.03	2.46	0	0.01	4.29	57.46 ± 2.34	51.46 ± 3.06
15	0	0	0	0	0	0	0	0	0	0	0	0	0	0	10.88	0	10.88	100 ± 0.00	100 ± 0.00
16	0	0	0	0	0	0	0.15	0	0	0.15	0	0.05	0	0	0	12.53	12.89	97.21 ± 1.04	92.76 ± 1.17
Total	1.95	9.15	1.47	2.25	4.94	1.04	13.87	9.18	8.35	9.16	0.91	7.95	0.59	4.79	10.88	13.50	100		

Table 2-6. Error matrix derived through accuracy assessment of the 2014 AST product. The surface types are numbered the same way as shown in Table 1-2.

		Reference																	Total (%)	User's accuracy (%)	Producer's accuracy (%)
		1	2	3	4	5	6	7	8	9	10	11	12	13	14	15	16	17			
Map	1	2.04	0.01	0.06	0.05	0.29	0.01	0.01	0.23	0.04	0.07	0.02	0.01	0	0.01	0	0	0.01	2.86	71.3 ± 2.9	72.6 ± 3.4
	2	0	8.46	0	0.09	0.05	0	0	0.4	0.08	0.02	0	0.06	0	0.12	0	0	0	9.28	91.2 ± 1.2	92.6 ± 1.1
	3	0.05	0	1.08	0	0.13	0	0.01	0.09	0	0.02	0.02	0	0	0	0	0	0	1.41	76.7 ± 3.9	68.7 ± 4.7
	4	0	0.01	0.01	0.95	0.05	0	0	0.09	0.03	0	0	0	0	0.02	0	0	0	1.14	82.8 ± 2.8	42.8 ± 3.4
	5	0.2	0.17	0.21	0.64	3.52	0.03	0.02	0.59	0.15	0.02	0.03	0	0.02	0.33	0	0	0.02	5.95	59.2 ± 2.6	76.2 ± 2.6
	6	0	0	0	0	0	0.05	0	0	0	0.01	0	0	0	0	0	0	0	0.07	70.0 ± 6.0	3.6 ± 0.8
	7	0.22	0.02	0.07	0.05	0.19	0.48	11.64	0.51	0.36	1.24	0.17	0.36	0.02	0.15	0	0.48	0.02	16.00	72.7 ± 1.7	83.9 ± 1.8
	8	0.26	0.17	0.06	0.28	0.17	0.09	0.3	4.84	0.58	0.11	0.07	0.09	0.01	0.44	0	0	0.02	7.50	64.6 ± 1.9	57.5 ± 2.2
	9	0	0.16	0.03	0.05	0.05	0.46	0.24	1.02	5.25	0.13	0.03	0.22	0.05	0.38	0	0	0	8.08	65.0 ± 2.8	71.9 ± 2.4
	10	0.02	0	0.04	0.02	0.06	0.23	0.79	0.19	0.21	6.37	0	0.48	0.02	0.21	0	0.23	0.01	8.90	71.5 ± 1.7	72.1 ± 2.1
	11	0.01	0.02	0	0	0.01	0.01	0.06	0.05	0.06	0.01	0.48	0.01	0	0	0	0	0	0.73	65.0 ± 6.2	57.3 ± 7.5
	12	0.01	0.01	0	0	0.04	0.02	0.07	0.05	0.16	0.46	0.01	6.97	0.08	0.55	0	0	0.02	8.44	82.6 ± 1.2	79.7 ± 1.7
	13	0	0	0	0	0	0	0.01	0.01	0	0	0	0.04	0.35	0.01	0	0	0	0.42	81.7 ± 3.6	58.9 ± 6.7
	14	0	0.1	0.02	0.06	0.05	0.01	0.06	0.34	0.39	0.18	0	0.41	0.03	2.7	0	0.01	0	4.35	62.0 ± 2.1	53.9 ± 2.7
	15	0	0	0	0	0	0	0.17	0	0	0	0	0	0	0	10.19	0	0	10.36	98.3 ± 1.7	100.0 ± 0.0
	16	0	0	0	0	0	0	0.49	0	0	0.18	0	0.09	0	0.09	0	12.53	0	13.37	93.7 ± 1.4	94.5 ± 0.9
	17	0	0	0	0	0	0	0	0	0	0.02	0	0	0	0	0	0	1.11	1.13	98.3 ± 1.7	91.3 ± 3.2
	Total	2.81	9.13	1.57	2.21	4.62	1.4	13.87	8.42	7.31	8.83	0.83	8.75	0.59	5.01	10.19	13.26	1.21	100		

2.8. Synergy of Continuity Missions for Surface Type Monitoring

VIIRS is designed to provide continuous global observations through continuity JPSS missions. With the successful launch of JPSS-1 in 2017, which was soon renamed NOAA-20, two identical VIIRS instruments are deployed on two orbiting satellites – S-NPP and NOAA-20. The two satellites share the same orbit, but their local overpass times differ by about 50 minutes. As a result, same day observations provided by the two satellites over the same ground location have different solar illumination geometry, and their viewing angles can differ by as much as 60 degrees (Figure 2-15, left). Because of these differences in illumination and viewing geometry, same day reflectance values provided by the two satellites are not identical even for the same area. However, those values are often highly correlated when there is no cloud and shadow (Figure 2-15, right).
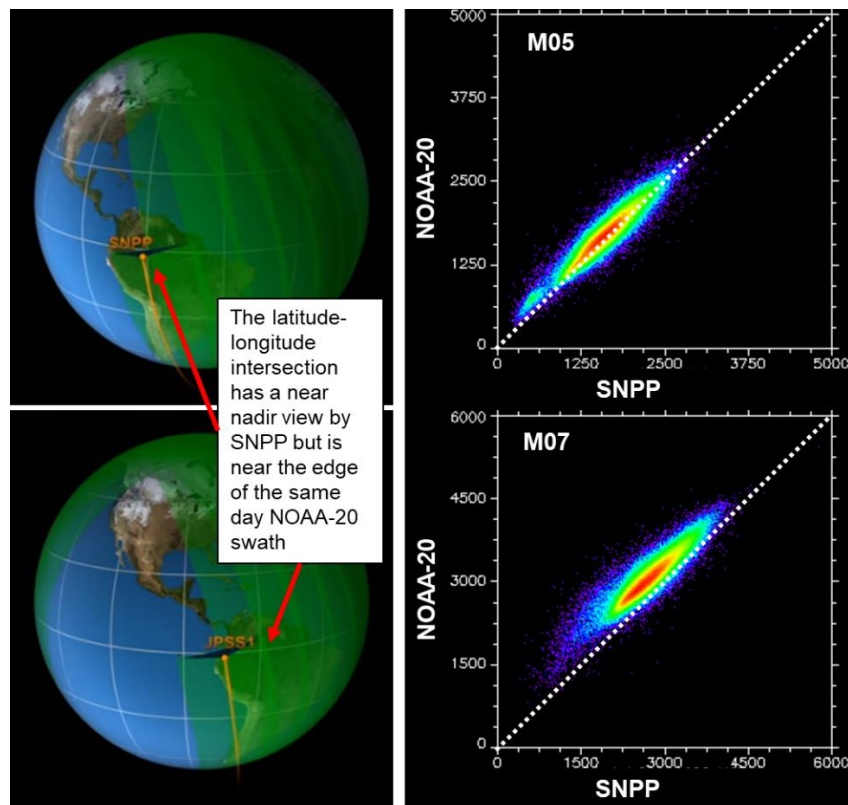
Figure 2-15. Left: NOAA-20 (formerly known as JPSS-1) and S-NPP share the same orbit, but their local overpass time differ by about 50 minutes, resulting in large differences in the viewing geometry of observations acquired by the two satellites over the same ground location. Right: Density plot (increasing number of points from blue to red) of same day reflectance data acquired on June 28, 2019 by the two satellites over a cloud free area in southwest Africa.

For VIIRS Surface Type mapping, the daily surface reflectance data are first aggregated to create monthly composites and then annual metrics (see sections 2.3.2.1-2.3.2.2). The annual metrics are then classified to produce the AST product. By April 2020, NOAA-20 accumulated its first set of observations over a 12-month period, which is required for generating the AST product. With the daily surface reflectance values from NOAA-20 and S-NPP being correlated but not identical, the monthly composites and annual metrics derived from these two satellites are also correlated but not identical (Figure 2-16). The AST maps derived using annual observations acquired between May 2019 and April 2020 by the two satellites are near identical. The maps derived from NOAA-20 and S-NPP had overall accuracies of 77.5±0.6% and 77.7±0.6% respectively.
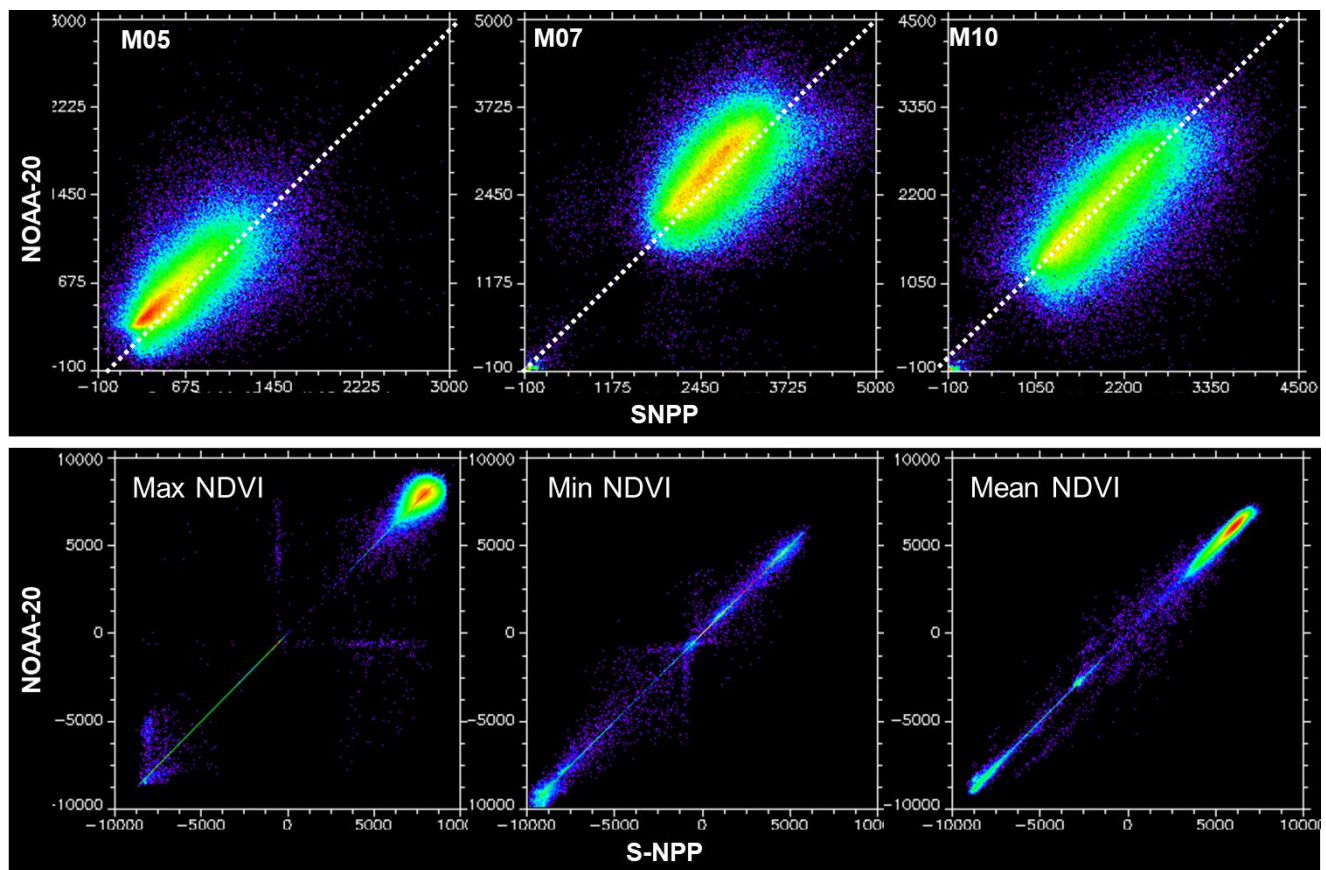
Figure 2-16. Comparison of monthly composites (upper row, May 2019) and annual metrics (lower row, see Table 2-4 for metrics definitions) derived from NOAA-20 and S-NPP. The blue to red color spectrum represents increasing number of points.

The two satellites can complement each other for monitoring sub-annual surface type dynamics. Together, they can provide more clear view observations for any given day than each satellite alone. This is because clouds and their shadows observed by one satellite

may disappear or move away when the other satellite passes 50 minutes later (Figure 2-17, right). Further, VIIRS data acquired by a single satellite may have gaps in some days due to practical reasons. When the locations of these gaps in the data acquired by the two satellites are not in the same regions, which is often the case, those gaps can be filled by creating daily mosaics using data from both satellites (Figure 2-17, left).
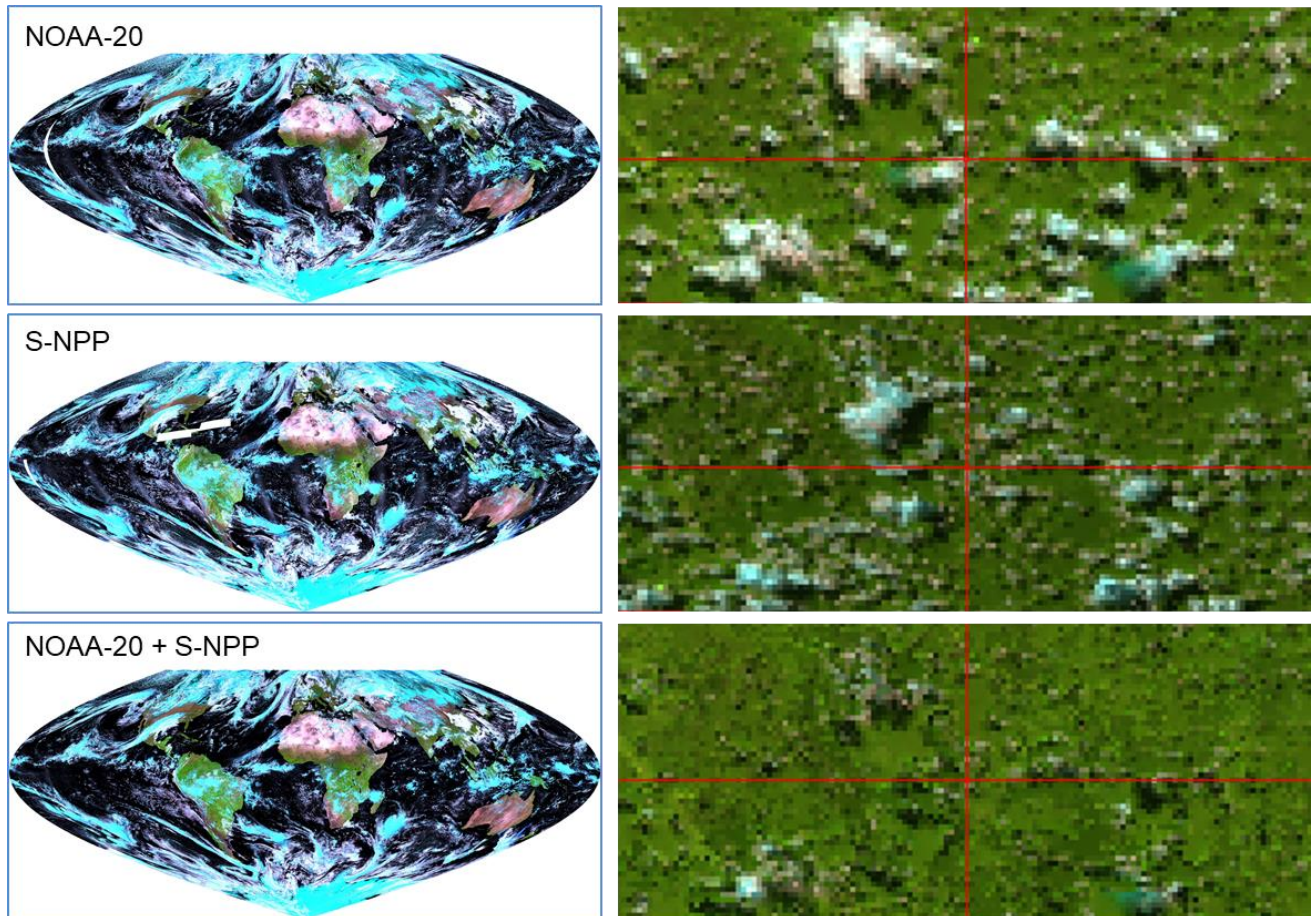
Figure 2-17. Left: Global daily mosaics created using NOAA-20 and S-NPP alone for January 1, 2020 have data gaps. Those gaps are filled when both satellites are used to create the daily mosaic. Right: A zoom-in view over South America where small clouds moved/changed a lot during the 50 minutes between the overpasses of the two satellites. The daily mosaic created using both satellites have substantially less clouds/shadow than those created using either satellite alone.

While the daily mosaics derived using both NOAA-20 and S-NPP still have substantial cloud cover across the globe (Figure 2-17, left), for many regions the two satellites can provide cloud free or near cloud free mosaics at temporal intervals short enough for tracking rapid surface type changes. For example, several fires in California burned

hundreds of thousands of acres in less than two weeks in August, 2020. Three-day composites derived using the two satellites provided near cloud free views over most of the land areas, making it possible to track the progressing of those fires (Figure 2-18).
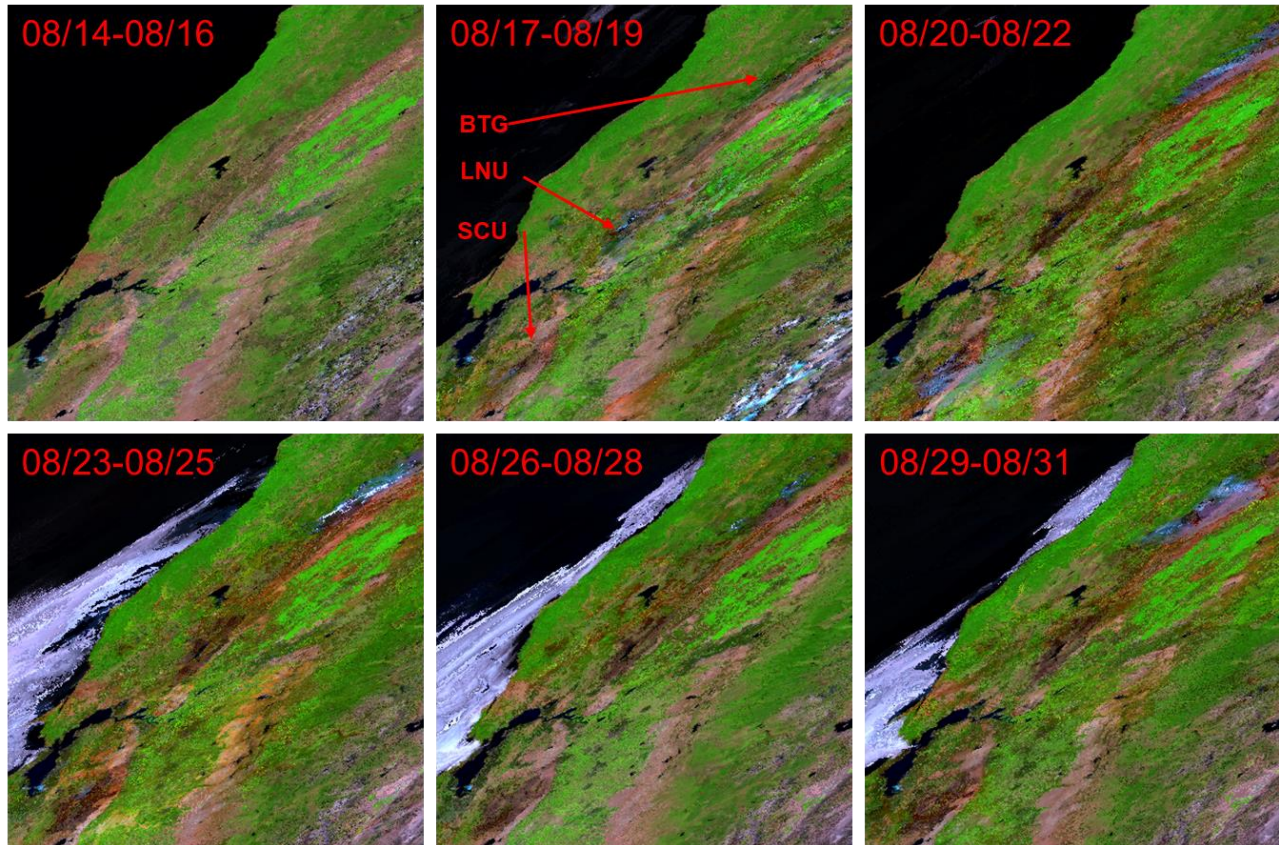
Figure 2-18. Three large fires in California burned a total of > 800,000 acres in less than two weeks in August 2020. Use of NOAA-20 and S-NPP together allowed derivation of near cloud free composites at 3-day composites for most land areas, which can be used to track the progressing of those fires.

In central Asia and other mid- to high latitude regions covered by seasonal snow in the winter, rapid snow melting in the spring can result in northward snow cover retreat of > 1000 km in less than one month. Use of both NOAA-20 and S-NPP allowed derivation of near cloud free composites at 5-day intervals for this region (Figure 2-19). These composites reveal that the majority of the melting occurred between 3/25/2020 and 4/6/2020. Such spatially and temporally detailed characterization of rapid snow cover change would not be possible using the monthly composites generated through the standard AST processing flow (see Figure 2-1) using a single satellite.
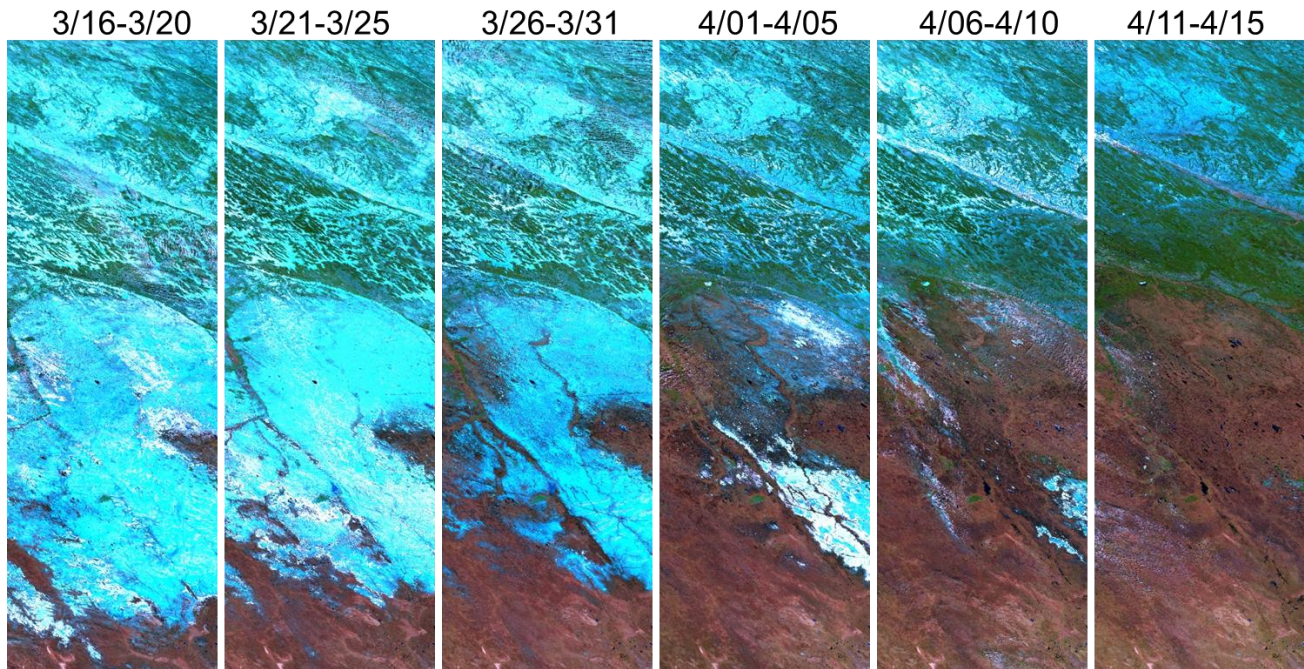
Figure 2-19. Much of the central Asia dryland was covered by snow until late March, 2020. The snow cover retreated northward by > 1000 km in less than 15 days (the size of the area shown is 600 km by 1800 km), which was captured by near cloud free 5-day composites created using VIIRS data from both NOAA-20 and S-NPP.

It should be noted that the benefits from using both NOAA-20 and S-NPP as compared to using either satellite alone to create short term composites diminish as the compositing length increases. This is because cloud contamination in longer term (e.g., monthly) composites derived using a single satellite is already very low. Further cloud reduction is achievable only over extremely cloudy regions where residual clouds exist in the composite created using a single satellite (Figure 2-20). Created using observations acquired over a 12-month period, many annual metrics are not affected by residual cloud/shadow contaminations. Visually, metrics created using either NOAA-20 or S-NPP, or both, look near identical (Figure 2-21). The AST map derived using VIIRS data acquired by both satellites from May 2019 to April 2020 had an overall accuracy of 78.0±0.6%, which as expected was only marginally better than the 77.5±0.6% overall accuracy from NOAA-20 and 77.7±0.6% from S-NPP. Derived using VIIRS observations acquired by both S-NPP and NOAA-20 from January 1, 2021 to December 31, 2021, the 2021 AST product had a slightly better overall accuracy of 79.3 ± 0.6% (Table 2-7).

NOAA-20	S-NPP	NOAA-20 + S-NPP
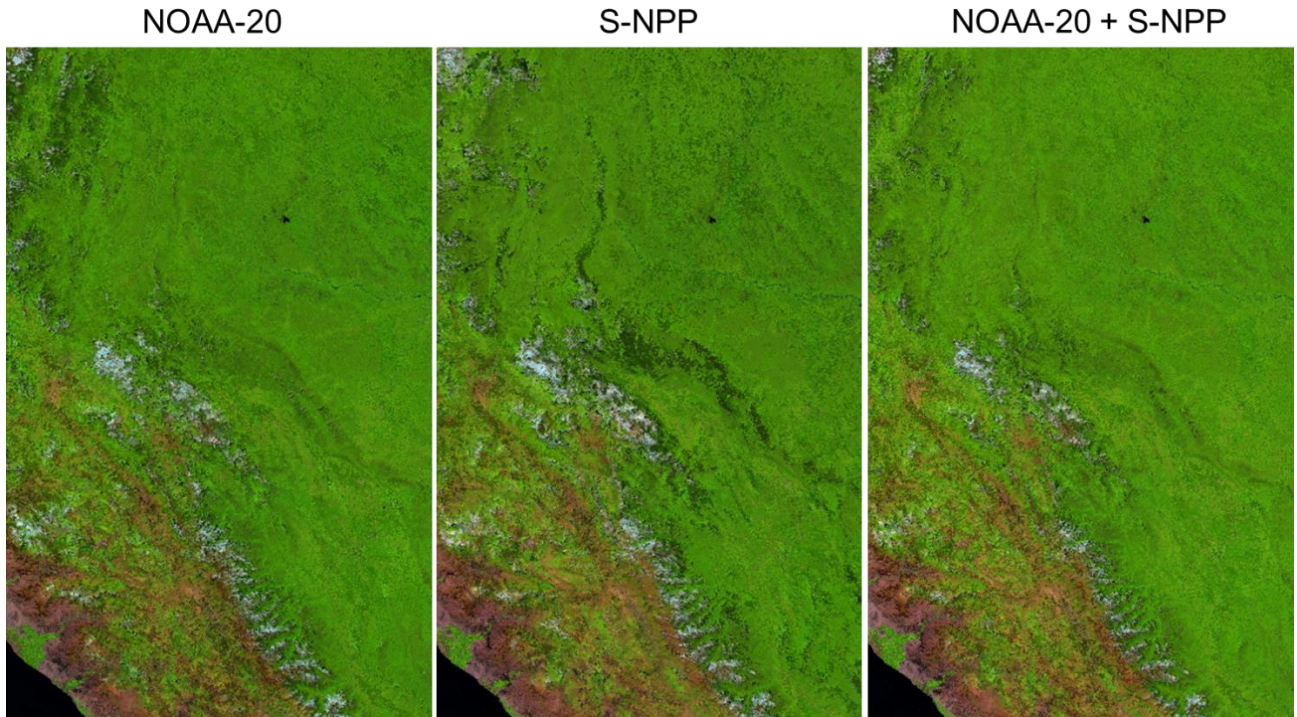
Figure 2-20. Monthly composites created using VIIRS data acquired by NOAA-20 or S-NPP in April 2020 over an extremely cloudy tropical South American area have substantial residual cloud contaminations, which are reduced in the composite created using both satellites.

NOAA-20	S-NPP	NOAA-20 + S-NPP

Figure 2-21. The annual mean NDVI images created using VIIRS data acquired between May 2019 and April 2020 by NOAA-20, S-NPP, and both, are near identical.

Table 2-7. Error matrix derived through accuracy assessment of the 2021 AST product. The surface types are numbered the same way as shown in Table 1-2.

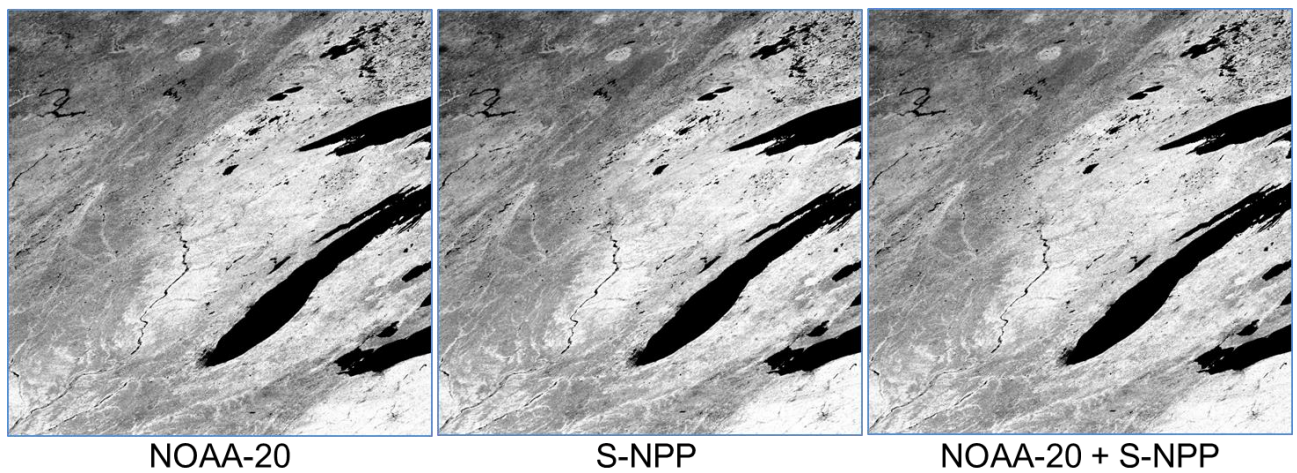| `										Reference									
AST	1	2	3	4	5	6	7	8	9	10	11	12	13	14	15	16	17	total	U Acc
1	2.09	0.03	0.06	0.05	0.28	0.00	0.01	0.23	0.04	0.00	0.03	0.01	0.01	0.03	0.00	0.00	0.01	2.86	72.93
2	0.00	8.46	0.00	0.08	0.12	0.00	0.00	0.39	0.09	0.03	0.00	0.05	0.02	0.05	0.00	0.00	0.00	9.28	91.14
3	0.04	0.00	1.09	0.00	0.11	0.00	0.04	0.11	0.01	0.00	0.01	0.00	0.00	0.00	0.00	0.00	0.00	1.41	77.39
4	0.00	0.00	0.01	0.95	0.07	0.00	0.00	0.09	0.02	0.00	0.00	0.00	0.00	0.01	0.00	0.00	0.00	1.14	82.94
5	0.19	0.12	0.31	0.75	3.69	0.00	0.00	0.61	0.07	0.00	0.00	0.02	0.02	0.17	0.00	0.00	0.00	5.95	61.99
6	0.00	0.00	0.00	0.00	0.00	0.04	0.01	0.01	0.00	0.01	0.00	0.00	0.00	0.00	0.00	0.00	0.00	0.07	50.67
7	0.21	0.07	0.09	0.05	0.14	0.07	11.85	0.66	0.32	1.37	0.27	0.25	0.05	0.11	0.00	0.46	0.05	16	74.07
8	0.23	0.19	0.04	0.26	0.15	0.01	0.30	5.34	0.54	0.10	0.06	0.03	0.03	0.21	0.00	0.00	0.01	7.5	71.24
9	0.03	0.21	0.00	0.08	0.05	0.13	0.34	1.24	4.92	0.18	0.03	0.39	0.00	0.52	0.00	0.00	0.00	8.08	60.83
10	0.08	0.01	0.00	0.03	0.06	0.08	0.82	0.29	0.29	6.43	0.00	0.50	0.01	0.08	0.00	0.23	0.01	8.9	72.23
11	0.01	0.00	0.00	0.00	0.01	0.00	0.06	0.04	0.07	0.01	0.52	0.00	0.00	0.00	0.00	0.00	0.00	0.73	71.19
12	0.01	0.01	0.01	0.02	0.05	0.02	0.07	0.06	0.17	0.43	0.02	7.06	0.07	0.44	0.00	0.00	0.01	8.44	83.64
13	0.00	0.00	0.00	0.00	0.00	0.00	0.00	0.00	0.00	0.00	0.00	0.03	0.38	0.01	0.00	0.00	0.00	0.42	89.23
14	0.00	0.13	0.02	0.09	0.06	0.02	0.07	0.43	0.45	0.17	0.00	0.23	0.02	2.64	0.00	0.01	0.01	4.35	60.78
15	0.00	0.00	0.00	0.00	0.00	0.00	0.17	0.00	0.00	0.17	0.00	0.00	0.00	0.00	10.02	0.00	0.00	10.36	96.72
16	0.00	0.00	0.00	0.00	0.00	0.00	0.32	0.00	0.00	0.14	0.00	0.05	0.00	0.05	0.00	12.78	0.05	13.37	95.61
17	0.02	0.00	0.00	0.00	0.00	0.02	0.00	0.00	0.02	0.00	0.00	0.00	0.02	0.00	0.00	0.00	1.06	1.13	93.75
total	2.88	9.22	1.63	2.35	4.78	0.37	14.06	9.5	7	9.04	0.94	8.61	0.61	4.31	10.02	13.47	1.21		
P Acc	72.31	91.7	66.99	40.29	77.13	9.53	84.32	56.26	70.2	71.15	55.08	82.05	61.37	61.34	100	94.88	87.92		

3.   ASSUMPTIONS AND LIMITATIONS

The VIIRS AST algorithm is designed based on a number of assumptions, including:

- The Earth's surface can be divided into discrete grid cells where each grid cell contains one and only one of the 17 IGBP surface types;
- The spectral-temporal information collected by VIIRS provides reasonable separability among the surface types across the globe;
- The surface type of each grid cell does not change within a calendar year.

These assumptions are not 100% valid. In fact, most grid cells at the 1-km resolution are mixtures of multiple land cover types. Some surface types are not separable using spectral-temporal information in certain regions. For example, wetlands are highly mixed and are often confused with other surface types. Grasslands and cereal/crops may not be separable in certain regions. Rice paddies as croplands many be confused with some wetlands. Tables 2-4 and 2-5 provide quantitative measures of the confusions among the 17 IGBP classes in the 2012 and 2014 AST products.

Further, many grid cells have surface type change within a year, which can be caused by events driven by both natural processes and human activities. For example, large portions of the Earth's surface have seasonal changes in snow cover (Figure 3-1). Short term changes in surface inundation occur in many areas during flooding events. More permanent changes in forest cover can result from wildfires, deforestation, and urbanization. The current AST product is not designed to capture such changes.

3.1. Performance Assumptions

Performance assessment of the VIIRS AST algorithm derived in section 2.7 assumes that all reference samples described in section 2.2 have been labeled correctly. This is not entirely true. Determining the surface type of a sample located in a homogeneous area may be relatively straightforward. For samples located in heterogeneous areas or near or along the edge or transition areas between different surface types, however, it can be difficult to determine their surface types reliably. Even human experts may not be able to label such samples correctly and consistently. It is not uncommon that different analysts label such samples differently (Feng et al. 2016; Montesano et al. 2009).
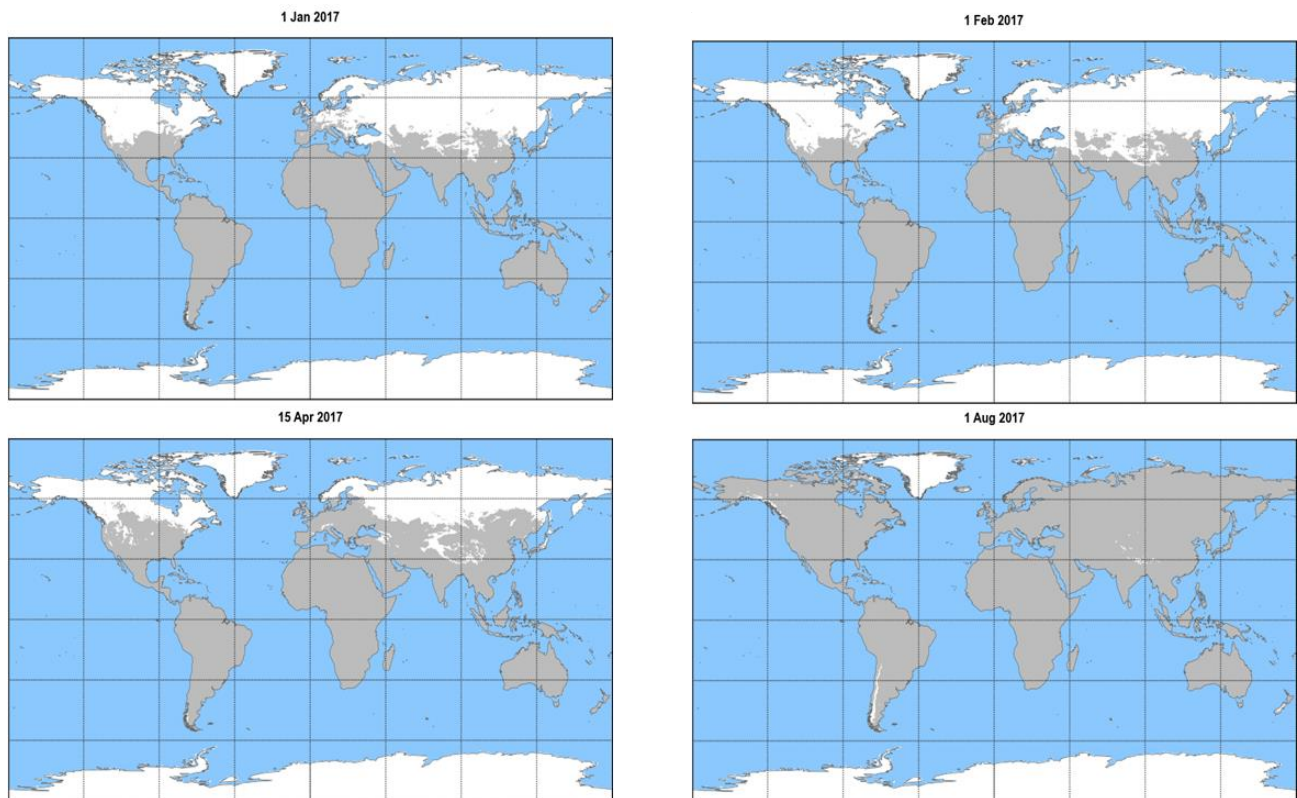
Figure 3-1. Snow flags in the Surface Type EDR generated by the IDPS system show that season snow cover changes between spring, summer, fall, and winter occur over large portions of the Earth's surface.

3.2. Potential Improvements

Given the limitations of the current VIIRS AST algorithm discussed above, the VIIRS surface type can be improved in many ways. Priorities should be given to improvements that can account for changes important for weather and climate studies. It has been demonstrated in many studies that surface type changes can result in changes in key climate variables (Li et al. 2017; Mahmood et al. 2014). For example, deforestation can cause changes in local surface temperature and precipitation (Winckler et al. 2017), while changes in surface inundation often result in changes in evapotranspiration (Zhao and Liu 2016). Agricultural expansion may result in warming over the Amazon but may produce cooling effects in the mid-latitudes (Feddema et al. 2005).

Capabilities that can account for some surface type changes already exist or are being developed. Use of MODIS data to detect surface type change has been explored in many studies (e.g. Guindon et al. 2014; Jin and Sader 2005; Mildrexler et al. 2009). Members of

the VIIRS surface type team implemented and evaluated the change vector analysis (CVA) and several other methods for detecting surface type changes using MODIS data (Zhan et al. 2000; Zhan et al. 2002). They have extensive experiences in developing fully automated methods for mapping forest change using Landsat data (Huang et al. 2010; Huang et al. 2008) and generating forest change products at national (Goward et al. 2015; Huang et al. 2009; Huang et al. 2007; Zhao et al. 2018), continental (Masek et al. 2008), and global scales (Feng et al. 2016; Kim et al. 2014). Further, the VIIRS Snow EDR can provide information on daily changes in snow cover. Algorithms developed through prove-ground studies on surface inundation and flood mapping using VIIRS data can be used to track short term changes in surface inundation. The VIIRS Active Fire product can be used to track fire occurrence, although additional research is needed to determine whether surface type changes occurred following each detected fire event. The feasibility to map surface type changes due to flooding and fire has been demonstrated in prototype studies conducted by the surface type team (Figure 3-2).

The effectiveness of the VIIRS data for detecting sub-km scale changes may be constrained by the 1-km grid cell size of the M bands used to generate the AST product. Detection of such changes requires that surface type be quantified as continuous fields within each grid cell. Algorithms for generating global continuous fields land cover products have been developed for MODIS and AVHRR (DeFries et al. 2000; Hansen et al. 2003). It has been demonstrated that such continuous fields products can be used to quantify subpixel forest loss using time series analysis methods (Song et al. 2014b). Use of the 375 m imagery bands should also improve the detectability of sub-km surface type changes.

Additional research is needed to improve the maturity of existing algorithms or develop more efficient algorithms suitable for routine monitoring of major surface type changes using VIIRS data, including data from both NOAA-20 and S-NPP. It would be relatively straightforward to combine a derived change product, once generated, with the AST product to create a daily surface type product suite. Such a product suite would be similar to the original surface type EDR in design, but should capture more change processes and therefore provide a more realistic representation of global surface cover conditions on a daily basis than the AST alone. Since models often require data to have geographic coordinates or a commonly used projection, this product suite should be produced in a gridded space that has needed georeferenced information. A future system that could be used to produce such a product suite is shown in Figure 3-3.
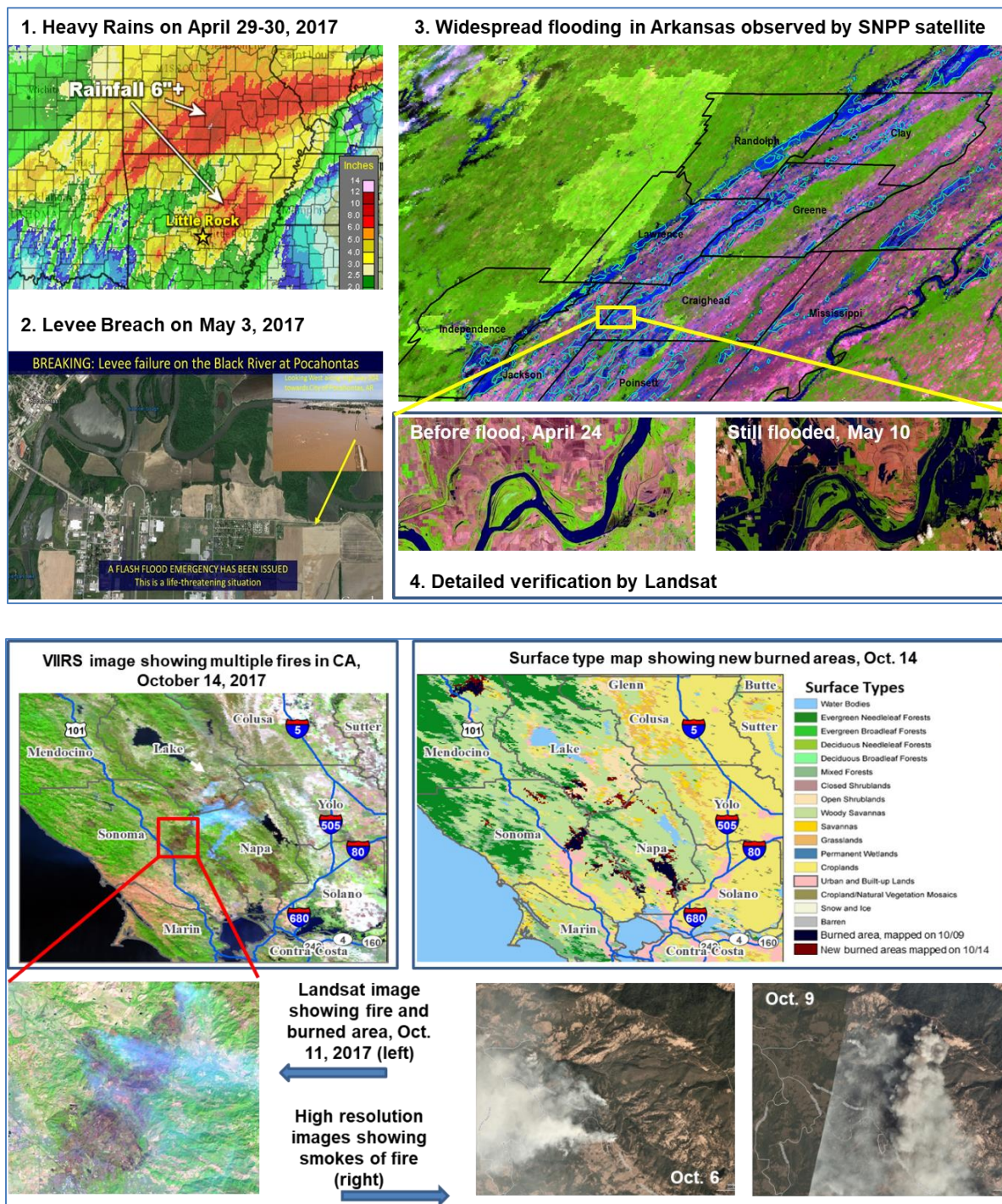
Figure 3-2. Selected prototype studies demonstrating the feasibility to map surface type changes caused by flooding (top) and fire (bottom) using VIIRS observations.
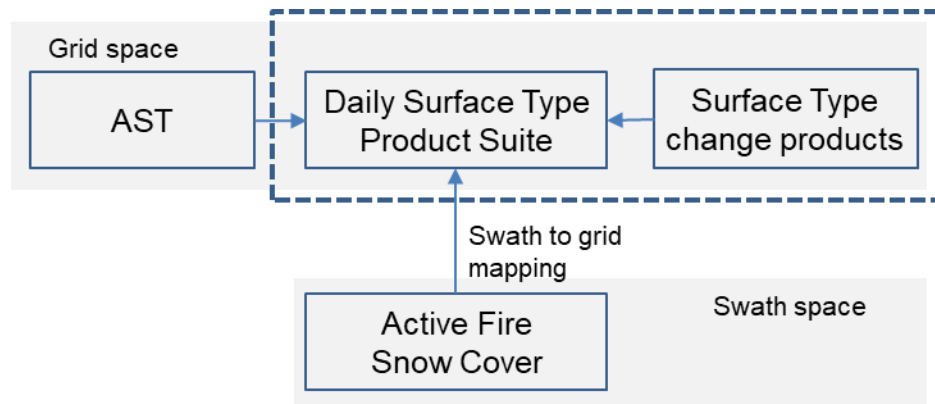
Figure 3-3. A conceptual framework of a future system that could be used to generate a daily VIIRS surface type product suite. Components in the dashed box can be developed in the future when needed resources become available.

4. REFERENCES

Bartholome, E., & Belward, A.S. (2005). GLC2000: a new approach to global land cover mapping from Earth observation data. *International Journal of Remote Sensing, 26*, 1959-1977.

Bauer, E., & Kohavi, R. (1998). An empirical comparison of voting classification algorithms: bagging, boosting, and variants. *Machine Learning, 5*, 1-38.

Belward, A., & Loveland, T. (1996). The DIS 1 km land cover data set. *Global Change News Letter, 27*, 7-9.

Bian, J., Li, A., Huang, C., Zhang, R., & Zhan, X. (2018). A self-adaptive approach for producing clear-sky composites from VIIRS surface reflectance datasets. *ISPRS Journal of Photogrammetry and Remote Sensing, 144*, 189-201.

Bright, R.M. (2015). Metrics for Biogeophysical Climate Forcings from Land Use and Land Cover Changes and Their Inclusion in Life Cycle Assessment: A Critical Review. *Environmental Science & Technology, 49*, 3291-3303.

Burges, C.J.C. (1998). A tutorial on support vector machines for pattern recognition. *Data Mining and Knowledge Discovery, 2*, 121-167.

Campagnolo, M.L., Sun, Q., Liu, Y., Schaaf, C., Wang, Z., & Román, M.O. (2016). Estimating the effective spatial resolution of the operational BRDF, albedo, and nadir reflectance products from MODIS and VIIRS. *Remote Sensing of Environment, 175*, 52-64.

Carroll, M.L., Townshend, J.R., DiMiceli, C.M., Noojipady, P., & Sohlberg, R.A. (2009). A new global raster water mask at 250 m resolution. *International Journal of Digital Earth, 2*, 291-308.

Chan, J.C.-W., Huang, C., & DeFries, R.S. (2001). Enhanced algorithm performance for land cover classification using bagging and boosting. *IEEE Transactions on Geoscience and Remote Sensing, 39*, 693-695.

Chan, J.C.-W., & Paelinckx, D. (2008). Evaluation of Random Forest and Adaboost tree-based ensemble classification and spectral band selection for ecotope mapping using airborne hyperspectral imagery. *Remote Sensing of Environment, 112*, 2999-3011.

Chen, F., & Dudhia, J. (2001). Coupling an advanced land surface-hydrology model with the Penn State-NCAR MM5 modeling system. Part I: Model Implementation and Sensitivity. *Monthly Weather Review, 129*, 569 -585.

Chen, J., Chen, J., Liao, A., Cao, X., Chen, L., Chen, X., He, C., Han, G., Peng, S., Lu, M., Zhang, W., Tong, X., & Mills, J. (2015). Global land cover mapping at 30 m resolution: A POK-based operational approach. *ISPRS Journal of Photogrammetry and Remote Sensing, 103*, 7-27.

Chuvieco, E., Ventura, G., MartÃn, M.P., & GÃ³mez, I. (2005a). Assessment of multitemporal compositing techniques of MODIS and AVHRR images for burned land mapping. *Remote Sensing of Environment, 94*, 450-462.

Chuvieco, E., Ventura, G., Martin, M.P., & Gomez, I. (2005b). Assessment of multitemporal compositing techniques of MODIS and AVHRR images for burned land mapping. *Remote Sensing of Environment, 94*, 450-462.

DeFries, R., Hansen, M., Townshend, J.R.G., Janetos, A.C., & Loveland, T.R. (2000). Continuous Fields 1 Km Tree Cover. In: College Park, Maryland: The Global Land Cover Facility.

DeFries, R.S., & Townshend, J.R.G. (1994). NDVI-derived land cover classifications at a global scale. *International Journal of Remote Sensing, 15*, 3567-3586.

DeFries, R.S., Townshend, J.R.G., & Hansen, M.C. (1999). Continuous fields of vegetation characteristics at the global scale at 1-km resolution. *Journal of Geophysical Research-Atmospheres, 104*, 16911-16923.

Dickinson, R.E. (1995). Land processes in climate models. *Remote Sensing of Environment, 51*, 27-38.

Feddema, J.J., Oleson, K.W., Bonan, G.B., Mearns, L.O., Buja, L.E., Meehl, G.A., & Washington, W.M. (2005). The Importance of Land-Cover Change in Simulating Future Climates. *Science, 310*, 1674-1678.

Feng, M., Sexton, J.O., Huang, C., Anand, A., Channan, S., Song, X.-P., Song, D.-X., Kim, D.-H., Noojipady, P., & Townshend, J.R. (2016). Earth science data records of global forest cover and change: Assessment of accuracy in 1990, 2000, and 2005 epochs. *Remote Sensing of Environment, 184*, 73-85.

Foody, G.M., & Arora, M.K. (1997). An evaluation of some factors affecting the accuracy of classification by an artificial neural network. *International Journal of Remote Sensing, 18*, 799-810.

Franklin, S.E., & Wulder, M.A. (2002). Remote sensing methods in medium spatial resolution satellite data land cover classification of large areas. *Progress in Physical Geography: Earth and Environment, 26*, 173-205.

Frantz, D., Röder, A., Stellmes, M., & Hill, J. (2017). Phenology-adaptive pixel-based compositing using optical earth observation imagery. *Remote Sensing of Environment, 190*, 331-347.

Friedl, M.A., Brodley, C.E., & Strahler, A.H. (1999). Maximizing land cover classification accuracies produced by decision trees at continental to global scales. *IEEE Transactions on Geoscience and Remote Sensing, 37*, 969-977.

Friedl, M.A., Sulla-Menashe, D., Tan, B., Schneider, A., Ramankutty, N., Sibley, A., & Huang, X. (2010). MODIS Collection 5 global land cover: Algorithm refinements and characterization of new datasets. *Remote Sensing of Environment, 114*, 168-182.

Friedl, M.A., Zhang, X.Y., Muchoney, D., Strahler, A.H., Woodcock, C.E., Gopal, S., Schneider, A., Cooper, A., Baccini, A., Gao, F., Schaaf, C., McIver, D.K., & Hodges, J.C.F. (2002). Global land cover mapping from MODIS: Algorithms and early results. *Remote Sensing of Environment, 83*, 287-302.

Gong, P., Wang, J., Yu, L., Zhao, Y., Zhao, Y., Liang, L., Niu, Z., Huang, X., Fu, H., Liu, S., Li, C., Li, X., Fu, W., Liu, C., Xu, Y., Wang, X., Cheng, Q., Hu, L., Yao, W., Zhang, H., Zhu, P., Zhao, Z., Zhang, H., Zheng, Y., Ji, L., Zhang, Y., Chen, H., Yan, A., Guo, J., Yu, L., Wang, L., Liu, X., Shi, T., Zhu, M., Chen, Y., Yang, G., Tang, P., Xu, B., Giri, C., Clinton, N., Zhu, Z., Chen, J., & Chen, J. (2013). Finer resolution observation and monitoring of global land cover: first mapping results with Landsat TM and ETM+ data. *International Journal of Remote Sensing, 34*, 2607-2654.

Goward, S.N., Huang, C., Zhao, F., Schleeweis, K., Rishmawi, K., Lindsey, M., Dungan, J.L., & Michaelis, A. (2015). NACP NAFD Project: Forest Disturbance History from Landsat, 1986-2010. In U.o.M.-N. NEX (Ed.). http://daac.ornl.gov/cgi-bin/dsviewer.pl?ds_id=1290: ORNL DAAC, Oak Ridge, Tennessee, USA.

Griffiths, P., van der Linden, S., Kuemmerle, T., & Hostert, P. (2013). Pixel-Based Landsat Compositing Algorithm for Large Area Land Cover Mapping. *Ieee Journal of Selected Topics in Applied Earth Observations and Remote Sensing, 6*, 2088-2101.

Guindon, L., Bernier, P.Y., Beaudoin, A., Pouliot, D., Villemaire, P., Hall, R.J., Latifovic, R., & St-Amant, R. (2014). Annual mapping of large forest disturbances across Canada's forests using 250 m MODIS imagery from 2000 to 2011. *Canadian Journal of Forest Research, 44*, 1545-1554.

Hansen, M., DeFries, R.S., Townshend, J.R.G., & Sohlberg, R. (2000). Global land cover classification at 1 km spatial resolution using a classification tree approach. *International Journal of Remote Sensing, 21*, 1331-1364.

Hansen, M.C., DeFries, R.S., Townshend, J.R.G., Carroll, M., Dimiceli, C., & Sohlberg, R.A. (2003). Global Percent Tree Cover at a Spatial Resolution of 500 Meters: First Results of the MODIS Vegetation Continuous Fields Algorithm. *Earth Interactions, 7*, 1-15.

Hansen, M.C., & Loveland, T.R. (2012). A review of large area monitoring of land cover change using Landsat data. *Remote Sensing of Environment, 122*, 66-74.

Hansen, M.C., Sohlberg, R., Dimiceli, C., Carroll, M., Defries, R.S., & Townshend, J.R.G. (2002). Towards an operational MODIS continuous field of percent tree cover

algorithm: Examples using AVHRR and MODIS data. *Remote Sensing of Environment, 83*, 303-319.

Hansen, M.C., Townshend, J.R.G., Defries, R.S., & Carroll, M. (2005). Estimation of tree cover using MODIS data at global, continental and regional/local scales. *International Journal of Remote Sensing, 26*, 4359-4380.

Hasager, C.B., Nielsen, N.W., Jensen, N.O., Boegh, E., Christensen, J.H., Dellwik, E., & Soegaard, H. (2003). Effective Roughness Calculated from Satellite-Derived Land Cover Maps and Hedge-Information used in a Weather Forecasting Model. *Boundary-Layer Meteorology, 109*, 227-254.

Holben, B.N. (1986). Characteristics of maximum-value composite images from temporal AVHRR data. *International Journal of Remote Sensing, 7*, 1417-1434.

Homer, C., Huang, C., Yang, L., Wylie, B., & Coan, M. (2004). Development of a 2001 national land cover database for the United States. *Photogrammetric Engineering & Remote Sensing, 70*, 829-840.

Huang, C., Davis, L.S., & Townshend, J.R.G. (2002). An assessment of support vector machines for land cover classification. *International Journal of Remote Sensing, 23*, 725-749.

Huang, C., Goward, S.N., Masek, J.G., Thomas, N., Zhu, Z., & Vogelmann, J.E. (2010). An automated approach for reconstructing recent forest disturbance history using dense Landsat time series stacks. *Remote Sensing of Environment, 114*, 183-198.

Huang, C., Homer, C., & Yang, L. (2003). Regional forest land cover characterization using medium spatial resolution satellite data. In M. Wulder, & S. Franklin (Eds.), *Methods and Applications for Remote Sensing of Forests: Concepts and Case Studies* (pp. 389-410). Boston: Kluwer Academic Publishers.

Huang, C., Kim, S., Altstatt, A., Song, K., Townshend, J.R.G., Davis, P., Rodas, O., Yanosky, A., Clay, R., Tucker, C.J., & Musinsky, J. (2009). Assessment of Paraguay's forest cover change using Landsat observations. *Global and Planetary Change, 67*, 1-12.

Huang, C., Kim, S., Altstatt, A., Townshend, J.R.G., Davis, P., Song, K., Tucker, C.J., Rodas, O., Yanosky, A., Clay, R., & Musinsky, J. (2007). Rapid loss of Paraguay's Atlantic forest and the status of protected areas – a Landsat assessment. *Remote Sensing of Environment, 106*, 460-466.

Huang, C., & Song, K. (2012). Forest Cover Change Detection Using Support Vector Machines. In C.P. Giri (Ed.), *Remote Sensing of Land Use and Land Cover: Principles and Applications* (pp. 191-206). London: Taylor & Francis.

Huang, C., Song, K., Kim, S., Townshend, J.R.G., Davis, P., Masek, J., & Goward, S.N. (2008). Use of a dark object concept and support vector machines to automate forest cover change analysis. *Remote Sensing of Environment, 112*, 970-985.

Jin, S., & Sader, S.A. (2005). MODIS time-series imagery for forest disturbance detection and quantification of patch size effects. *Remote Sensing of Environment, 99*, 462-470.

Kim, D.-H., Sexton, J.O., Noojipady, P., Huang, C., Anand, A., Channan, S., Feng, M., & Townshend, J.R. (2014). Global, Landsat-based forest-cover change from 1990 to 2000. *Remote Sensing of Environment, 155*, 178-193.

Li, F., Lawrence, D.M., & Bond-Lamberty, B. (2017). Impact of fire on global land surface air temperature and energy budget for the 20th century due to changes within ecosystems. *Environmental Research Letters, 12*, 044014.

Loveland, T.R., Reed, B.C., Brown, J.F., Ohlen, D.O., Zhu, Z., Yang, L., & Merchant, J.W. (2000). Development of a global land cover characteristics database and IGBP DISCover from 1km AVHRR data. *International Journal of Remote Sensing, 21*, 1303-1330.

Luo, Y., Trishchenko, A.P., & Khlopenkov, K.V. (2008). Developing clear-sky, cloud and cloud shadow mask for producing clear-sky composites at 250-meter spatial resolution for the seven MODIS land bands over Canada and North America. *Remote Sensing of Environment, 112*, 4167-4185.

Luyssaert, S., Jammet, M., Stoy, P.C., Estel, S., Pongratz, J., Ceschia, E., Churkina, G., Don, A., Erb, K., Ferlicoq, M., Gielen, B., Grünwald, T., Houghton, R.A., Klumpp, K., Knohl, A., Kolb, T., Kuemmerle, T., Laurila, T., Lohila, A., Loustau, D., McGrath, M.J., Meyfroidt, P., Moors, E.J., Naudts, K., Novick, K., Otto, J., Pilegaard, K., Pio, C.A., Rambal, S., Rebmann, C., Ryder, J., Suyker, A.E., Varlagin, A., Wattenbach, M., & Dolman, A.J. (2014). Land management and land-cover change have impacts of similar magnitude on surface temperature. *Nature Climate Change, 4*, 389.

Mahmood, R., Pielke, R.A., Hubbard, K.G., Niyogi, D., Dirmeyer, P.A., McAlpine, C., Carleton, A.M., Hale, R., Gameda, S., Beltrán-Przekurat, A., Baker, B., McNider, R., Legates, D.R., Shepherd, M., Du, J., Blanken, P.D., Frauenfeld, O.W., Nair, U.S., & Fall, S. (2014). Land cover changes and their biogeophysical effects on climate. *International Journal of Climatology, 34*, 929-953.

Mantyka-Pringle, C.S., Martin, T.G., Moffatt, D.B., Udy, J., Olley, J., Saxton, N., Sheldon, F., Bunn, S.E., & Rhodes, J.R. (2016). Prioritizing management actions for the conservation of freshwater biodiversity under changing climate and land-cover. *Biological Conservation, 197*, 80-89.

Masek, J.G., Huang, C., Wolfe, R.E., Cohen, W., Hall, F., Kutler, J., & Nelson, P. (2008). North American forest disturbance mapped from a decadal Landsat record. *Remote Sensing of Environment, 112*, 2914-2926.

Mildrexler, D.J., Zhao, M., & Running, S.W. (2009). Testing a MODIS Global Disturbance Index across North America. *Remote Sensing of Environment, 113*, 2103-2117.

Montesano, P.M., Nelson, R., Sun, G., Margolis, H., Kerber, A., & Ranson, K.J. (2009). MODIS tree cover validation for the circumpolar taiga–tundra transition zone. *Remote Sensing of Environment, 113*, 2130-2141.

Mountrakis, G., Im, J., & Ogole, C. (2011). Support vector machines in remote sensing: A review. *ISPRS Journal of Photogrammetry and Remote Sensing, 66*, 247-259.

Muchoney, D., Strahler, A., Hodges, J., & LoCastro, J. (1999). The IGBP DISCover confidence sites and the system for terrestrial ecosystem parameterization. Tools for

validating global land-cover data. *Photogrammetric Engineering and Remote Sensing, 65*, 1061-1067.

Myneni, R.B., Nemani, R.R., & Running, S.W. (1997). Estimation of global leaf area index and absorbed par using radiative transfer models. *IEEE Geoscience and Remote Sensing, 35*, 1380-1393.

Olofsson, P., Foody, G.M., Herold, M., Stehman, S.V., Woodcock, C.E., & Wulder, M.A. (2014). Good practices for estimating area and assessing accuracy of land change. *Remote Sensing of Environment, 148*, 42-57.

Paola, J.D., & Schowengerdt, R.A. (1995). A review and analysis of backpropagation neural networks for classification of remotely sensed multi-spectral imagery. *International Journal of Remote Sensing, 16*, 3033-3058.

Quinlan, J.R. (1993). *C4.5 programs for machine learning*. San Mateo, California: Morgan Kaufmann Publishers.

Roy, D.P., Ju, J.C., Kline, K., Scaramuzza, P.L., Kovalskyy, V., Hansen, M., Loveland, T.R., Vermote, E., & Zhang, C.S. (2010). Web-enabled Landsat Data (WELD): Landsat ETM plus composited mosaics of the conterminous United States. *Remote Sensing of Environment, 114*, 35-49.

Salazar, A., Baldi, G., Hirota, M., Syktus, J., & McAlpine, C. (2015). Land use and land cover change impacts on the regional climate of non-Amazonian South America: A review. *Global and Planetary Change, 128*, 103-119.

Schneider, A., Friedl, M.A., & Potere, D. (2010). Mapping global urban areas using MODIS 500-m data: New methods and datasets based on 'urban ecoregions'. *Remote Sensing of Environment, 114*, 1733-1746.

Schueler, C.F., Lee, T.F., & Miller, S.D. (2013). VIIRS constant spatial-resolution advantages. *International Journal of Remote Sensing, 34*, 5761-5777.

Sellers, P.J., Meeson, B.W., Hall, F.G., Asrar, G., Murphy, R.E., Schiffer, R.A., Bretherton, F.P., & et al. (1995). Remote sensing of the land surface for studies of global change: models - algorithms - experiments. *Remote Sensing of Environment, 51*, 3-26.

Sellers, P.J., Randall, D.A., Collatz, G.J., Berry, J.A., Field, C.B., Dazlich, D.A., Zhang, C., Collelo, G.D., & Bounoua, L. (1996). A Revised Land Surface Parameterization (SiB2) for Atmospheric GCMS. Part I: Model Formulation. *Journal of Climate, 9*, 676-705.

Senapathi, D., Carvalheiro, L.G., Biesmeijer, J.C., Dodson, C.-A., Evans, R.L., McKerchar, M., Morton, R.D., Moss, E.D., Roberts, S.P.M., Kunin, W.E., & Potts, S.G. (2015). The impact of over 80 years of land cover changes on bee and wasp pollinator communities in England. *Proceedings of the Royal Society B: Biological Sciences, 282*.

Sexton, J.O., Noojipady, P., Song, X.-P., Feng, M., Song, D.-X., Kim, D.-H., Anand, A., Huang, C., Channan, S., & Pimm, S.L. (2016). Conservation policy and the measurement of forests. *Nature Climate Change, 6*, 192-196.

Song, X.-P., Huang, C., Feng, M., Sexton, J.O., Channan, S., & Townshend, J.R. (2014a). Integrating global land cover products for improved forest cover characterization: an application in North America. *International Journal of Digital Earth, 7*, 709-724.

Song, X.-P., Huang, C., Sexton, J., Channan, S., & Townshend, J. (2014b). Annual Detection of Forest Cover Loss Using Time Series Satellite Measurements of Percent Tree Cover. *Remote Sensing, 6*, 8878-8903.

Song, X.-P., Huang, C., & Townshend, J.R. (2017). Improving global land cover characterization through data fusion. *Geo-spatial Information Science*, 1-10.

Stehman, S.V. (1999). Basic probability sampling designs for thematic map accuracy assessment. *International Journal of Remote Sensing, 20*, 2423-2441.

Stehman, S.V., & Czaplewski, R.L. (1998). Design and analysis for thematic map accuracy assessment: fundamental principles. *Remote Sensing of Environment, 64*, 331-344.

Stow, D.A., Tinney, L.R., & Estes, J.E. (1980). Deriving land use/land cover change statistics from Landsat: a study of prime agricultural land. In, *Proceedings of the 14th International Symposium on Remote Sensing of Environment* (pp. 1227-1237). Ann Arbor.

Townshend, J.R.G. (1992). Land cover. *International Journal of Remote Sensing, 13*, 1319-1328.

Townshend, J.R.G., Justice, C., Li, W., Gurney, C., & McManus, J. (1991). Global land cover classification by remote sensing: present capabilities and future possibilities. *Remote Sensing of Environment, 35*, 243-255.

Townshend, J.R.G., Justice, C.O., Skole, D., Malingreau, J.-P., Teillet, J.C.P., Sadowski, F., & Ruttenberg, S. (1994). The 1 km resolution global data set: needs of the International Geosphere Biosphere Programme. *International Journal of Remote Sensing, 14*, 3417-3441.

Vapnik, V.N. (1995). *The nature of statistical learning theory*. New York: Springer.

Venter, O., Sanderson, E.W., Magrach, A., Allan, J.R., Beher, J., Jones, K.R., Possingham, H.P., Laurance, W.F., Wood, P., Fekete, B.M., Levy, M.A., & Watson, J.E.M. (2016). Sixteen years of change in the global terrestrial human footprint and implications for biodiversity conservation. *Nature Communications, 7*, 12558.

Wilson, M.F., & Henderson-Sellers, A. (1985). A global archive of land cover and soils data for use in general circulation climate models. *Journal of Climatology, 5*, 119-143.

Winckler, J., Reick, C.H., & Pongratz, J. (2017). Robust Identification of Local Biogeophysical Effects of Land-Cover Change in a Global Climate Model. *Journal of Climate, 30*, 1159-1176.

Wolfe, R.E., Roy, D.P., & Vermote, E. (1998). MODIS land data storage, gridding, and compositing methodology: Level 2 grid. *Geoscience and Remote Sensing, IEEE Transactions on, 36*, 1324-1338.

Wood, E.F. (1991). Global scale hydrology: advances in land surface modeling. In, *Reviews of Geophysics* (pp. 193-201).

Xue, Y., Zeng, F.J., Mitchell, K., Janjic, Z., & Rogers, E. (2001). The impact of land surface processes on the simulation of the U.S. hydrological cycle: A case study of 1993 US flood using the Eta/SSiB regional model. *Monthly Weather Review, 129*, 2833-2860.

Zhan, X., DeFries, R., Townshend, J.R.G., Dimiceli, C., Hansen, M., Huang, C., & Sohlberg, R. (2000). The 250m global land cover change product from the Moderate

Resolution Imaging Spectroradiometer of NASA's Earth Observing System. *International Journal of Remote Sensing, 21*, 1433-1460.

Zhan, X., Dimiceli, C., Carroll, M.L., Eastman, J.C., Hansen, M., DeFries, R., Townshend, J.R.G., & Sohlberg, R. (2002). Detection of land cover changes using MODIS 250 m data. *Remote Sensing of Environment, 83*, 336-350.

Zhang, R., Huang, C., Zhan, X., Dai, Q., & Song, K. (2016). Development and validation of the global surface type data product from S-NPP VIIRS. *Remote Sensing Letters, 7*, 51-60.

Zhang, R., Huang, C., Zhan, X., Jin, H., & Song, X.-P. (2017). Development of S-NPP VIIRS global surface type classification map using support vector machines. *International Journal of Digital Earth, 11*, 212-232.

Zhao, F., Huang, C., Goward, S.N., Schleeweis, K., Rishmawi, K., Lindsey, M.A., Denning, E., Keddell, L., Cohen, W.B., Yang, Z., Dungan, J.L., & Michaelis, A. (2018). Development of Landsat-based annual US forest disturbance history maps (1986–2010) in support of the North American Carbon Program (NACP). *Remote Sensing of Environment, 209*, 312-326.

Zhao, X., & Liu, Y. (2016). Evapotranspiration Partitioning and Response to Abnormally Low Water Levels in a Floodplain Wetland in China. *Advances in Meteorology, 2016*, 11.

Zhou, G., Wei, X., Chen, X., Zhou, P., Liu, X., Xiao, Y., Sun, G., Scott, D.F., Zhou, S., Han, L., & Su, Y. (2015). Global pattern for the effect of climate and land cover on water yield. *Nature Communications, 6*, 5918.

END OF DOCUMENT